Electronic Supplementary Material (ESI) for Chemical Science.
This journal is © The Royal Society of Chemistry 2023

# Supplementary Material: Can range-separated functionals be optimally tuned to predict spectra and excited state dynamics in photoactive iron complexes?

J. Patrick Zobel,[*,†] Ayla Kruse,[‡,¶] Stefan Lochbrunner,[‡,¶] Sergey I. Bokarev,[§,‡] Oliver Kühn,[‡] Leticia González,[†] and Olga S. Bokareva[*,‡,‖]

†*Institute of Theoretical Chemistry, Faculty of Chemistry, University of Vienna, Währingerstr. 19, 1090 Vienna, Austria*

‡*Institute of Physics, University of Rostock, Albert-Einstein-Straße 23-24, 18059 Rostock, Germany*

¶*Department of Life, Light and Matter, University of Rostock, Albert-Einstein-Straße 21, 18059 Rostock, Germany*

§*Chemistry Department, Technical University of Munich, Lichtenbergstr. 4, Garching 85748, Germany*

‖*Institute of Physics, University of Kassel, Heinrich-Plett-Straße 40, 34132 Kassel, Germany*

E-mail: jan.patrick.zobel@univie.ac.at; olga.bokareva@uni-rostock.de

# Contents

# S1 Computational Details

## S1.1 Optimal Tuning

The equilibrium geometries of $[Fe(cpmp)_2]^{2+}$in the ground, two lowest excited triplets states (of MC and MLCT character), and MC quintet state have been optimized using B3LYP[1]/ def2TZVP[2,3]. The obtained configurations were checked for the absence of imaginary frequencies by harmonic frequency analysis. To limit computational costs, the optimal tuning of the functional was done using the 6-31G(d) basis set[4,5] of moderate size. For selected cases, the tuning was repeated using the def2TZVP basis set, leading to very similar results.

To optimize the range-separation parameters for a given compound in some electronic state, single-point calculations on the ($\alpha$, $\omega$) grid were done with DFT (for closed-shell systems) or UDFT (for open-shell configurations). The analysis of Huang-Rhys factors was done with the VISPER program package (T. Möhle, University of Rostock).

The respective DFT and TDDFT calculations have been done with Gaussian[6] and QChem[7] program suites. The calculations for the "MC-tuning" were performed using the constrained SCF approach[8] as provided by the QChem program package.[7] The assignment of excited states was done based on the analysis of the density-matrix.[9] For the spectra, a phenomenological broadening by a Gaussian line shape (FWHM = 0.2 eV) was employed. Solvent effects (acetonitrile) for DFT/TDDFT calculations were included within the polarized continuum model (PCM) approach.[10] Note that the tuning of range-separation parameters was done in vacuum as it was shown previously[11,12] that tuning combined with the PCM model leads to the underestimation of the exact exchange percentage in the constructed functional.

The influence of the different geometries has been studied by us previously on the example of complexes $[Ir(bpy)(ppy)_2]^{2+}$ with triethylamine and different iron carbonyls[11]. Both mutual spatial orientation and the distance between IrPS and the second molecule have been varied. We have shown that only substantial changes in the distance between the complex' constituents (but not their mutual orientation) lead to notable changes in optimal parameters. Even if some variations of optimal parameters may take place, the tuning of the functional for each geometry of the subsystem may lead to size inconsistency or nonphysical potential energy curves in excited states[13,14].

## S1.2 Multi-reference calculations

The CASSCF/CASPT2 calculations were performed using OpenMolcas 18.09.[15] The active space (10e/12MO) was constructed from the following orbitals to account for both MC and MLCT states: three non-bonding $3d$-orbitals of the iron atom as well as three corresponding Rydberg-like $4d$ orbitals to include the double-shell effect, two $\sigma_d$-bonding and two $\sigma_d^*$-antibonding orbitals, and the two vacant $\pi^*$-orbitals of the ligands (see Figure 1b)). The highest possible Abelian point symmetry group $C_2$, Cholesky decomposition of the two-electron integral matrix[16] and extended relativistic ANO-RCC-TZVP[17,18] basis set together with Douglas-Kroll-Hess approach[19] for scalar relativistic effects or 6-31G(d) were utilized. State-averaging was performed over the 10 lowest states of given symmetry and multiplicity, and the frozen-core approximation was utilized at the CASPT2 level. A default IPEA shift[20] of 0.25 a.u. (and 0.50 for the purpose of comparison) and an additional imaginary shift[21] of 0.2 a.u. to cope with the intruder states problem have been applied. As different solvent models are implemented in various quantum-chemistry packages, the lowest electronic transitions computed with CASPT2 and TDDFT were compared both in vacuum (with a larger basis set ANO-RCC-TZVP) and in PCM solvent (with smaller basis set 6-31G(d)).

## S1.3 Excited-state dynamics simulations

The nonadiabatic dynamics were simulated using the trajectory surface hopping (SH) method on potentials parametrized with a linear vibronic coupling (LVC) model[22–24] —an efficient strategy to study the excited-state dynamics of transition-metal complexes.[25–28] For this purpose we used the SHARC approach[29–31] with the SHARC2.1 program package.[32] Two

LVC models were setup using the LC-BLYP functional[33] and different optimal values of the range-separation parameters ($\alpha$; $\omega$), i.e., set A (0.0; 0.14) and set B (0.2; 0.08), see Section 2. The LVC models comprise 11 singlet and 20 triplet (i.e. 71 total) states for set A and 9 singlet and 14 triplet (i.e. 51 total) states for set B, respectively, corresponding to the number of states in the energy range of the lowest-energy absorption band described with the different tuning parameters (see Figure 5). Quintet MC states have not been included into the model. Transient absorption data on this compound were assigned to an ultrafast MC population, but there were no spectroscopic signatures that could be used to differentiate between the multiplicities on that time scale. A possible reason could be, e.g. parallel running potential curves along the reaction coordinates. Hence we expect that differentiating between triplet and quintet MC states will not change our general conclusions for the few ps time range.

The LVC coupling elements were obtained numerically from TDDFT calculations on geometries displaced by ±0.05 units from the ground-state optimized geometry for each of the 213 normal modes of the molecule. Intrastate coupling constants were obtained as numerical gradients and interstate coupling constants were obtained from the change in the wavefunction overlaps.

TDDFT calculations were performed in the Tamm-Dancoff approximation (TDA)[34] using the ORCA4.2 program.[35] For both parametrizations, the 6-31G(d) basis set was used for all atoms.[36–39] Solvent effects of acetonitrile were included using the C-PCM model as implemented in ORCA4.2. Scalar relativistic effects were modelled using the zeroth-order regular approximation (ZORA) Hamiltonian.[40] For the self-consistent-field (SCF) calculations, the resolution-of-identity approximation (RIJCOSX), tight SCF convergence criteria (TightSCF), and the Grid4 integration grid were used.

SH/LVC dynamics simulations were performed for each of the LVC models using the pySHARC framework.[23] Initial nuclear coordinates and momenta were sampled from a Wigner distribution of 10.000 geometries around the Franck-Condon geometry.[41] For each Wigner ensemble, absorption spectra were calculated using the respective LVC model potentials. Initial excited states were selected stochastically within the energy range of the lowest-energy absorption band (1.0-2.5 eV) based on their oscillator strength.[42] 1000 trajectories were then propagated for a simulation time of 2000 fs using a nuclear time step of 0.5 fs and an electronic time step of 0.02 fs within the local diabatization method.[43] An energy-based decoherence correction with a constant of $C = 0.1$ a.u. was used.[44] During the surface hops, kinetic energy was adjusted by re-scaling the velocity vectors. Surface hopping probabilities were approximated using the wave function overlaps.[45]

# S2 Optimal tuning

## S2.1 General Strategy

The range-separation parameters $\alpha$ and $\omega$ have been tuned for the generalized form (Eq. S1) of the LC-BLYP functional based on the following partitioning of the Coulomb operator:[33]

$$\frac{1}{r_{12}} = \frac{1 - [\alpha + \beta \cdot \mathrm{erf}(\omega r_{12})]}{r_{12}} + \frac{\alpha + \beta \cdot \mathrm{erf}(\omega r_{12})}{r_{12}} . \tag{S1}$$

With this, the initial exchange kernel in DFT is complemented with the exact Hartree-Fock exchange, which has the correct asymptotic behavior. The $\omega$ parameter defines the switching rate, and its inverse is proportional to a characteristic interelectron distance. The second (dimensionless) parameter $\alpha$ sets a global $r_{12}$-independent exact-exchange contribution. We assume $\beta = 1-\alpha$ to ensure that the exact exchange cancels self-interaction completely. Thus, the range-separated part of the LC-BLYP functional depends on the parameters $(\alpha, \omega)$ that we can exploit for tuning. The particular functional LC-BLYP has been chosen for tuning, as it is the most similar one to the popular B3LYP that we have applied for the purpose of comparison. Note that other functionals like BNL or PBE could be a possible option too, see e.g. Refs. 46,47.

The tuning most commonly follows the ΔSCF method.[13,48,49] Here, the energetic positions of HOMO and LUMO of a given system are tuned to the IP and EA according to Koopmans' theorem. The LUMO can thereby be substituted with the HOMO of $N+1$-electron system. The IP and EA are computed as the differences between ground state (gs) energies of a given multiplicity with $N$ and $N \pm 1$ electrons, i.e.,

$$\mathrm{IP}^{\alpha,\omega}(N) = E_{\mathrm{gs}}^{\alpha,\omega}(N-1) - E_{\mathrm{gs}}^{\alpha,\omega}(N)\,, \tag{S2}$$

$$\mathrm{EA}^{\alpha,\omega}(N) = \mathrm{IP}^{\alpha,\omega}(N+1) = E_{\mathrm{gs}}^{\alpha,\omega}(N) - E_{\mathrm{gs}}^{\alpha,\omega}(N+1)\,. \tag{S3}$$

Two separate tuning functions are considered:

$$J_0(\alpha,\omega) = \left|\varepsilon_{\mathrm{HOMO}}^{\alpha,\omega}(N) + \mathrm{IP}^{\alpha,\omega}(N)\right|\,, \tag{S4}$$

$$J_1(\alpha,\omega) = \left|\varepsilon_{\mathrm{HOMO}}^{\alpha,\omega}(N+1) + \mathrm{EA}^{\alpha,\omega}(N)\right|\,. \tag{S5}$$

To ensure a proper description of the fundamental HOMO-LUMO gap, the functions $J_0(\alpha,\omega)$ and $J_1(\alpha,\omega)$ should be minimized simultaneously which leads to minimizing the general function

$$J^*(\alpha,\omega) = \sqrt{J_0^2(\alpha,\omega) + J_1^2(\alpha,\omega)}\,. \tag{S6}$$

Note that, in general, $J^*(\alpha,\omega)$ can be non-zero even for exact functionals, because it is defined for systems with different numbers of electrons.

For organometallic systems with conjugated ligands of the size of cpmp, typical $\omega$ values are in the range of 0.10-0.20, given that $\alpha$ is taken to be zero.[11,50–59]. Concerning the constant exchange contribution, different functionals suggest numbers between 0 and 100%. In general, the larger $\alpha$ is for optimal parameters, the smaller $\omega$ will be. Thus, if enough constant exchange is added, the variable distance-dependent exchange contribution is less important. However, if we take $\alpha$ to be 0.30, for instance, the physical significance of $\omega$, i.e., of the range-dependent exchange, is minute. That is why in this study, we focus on

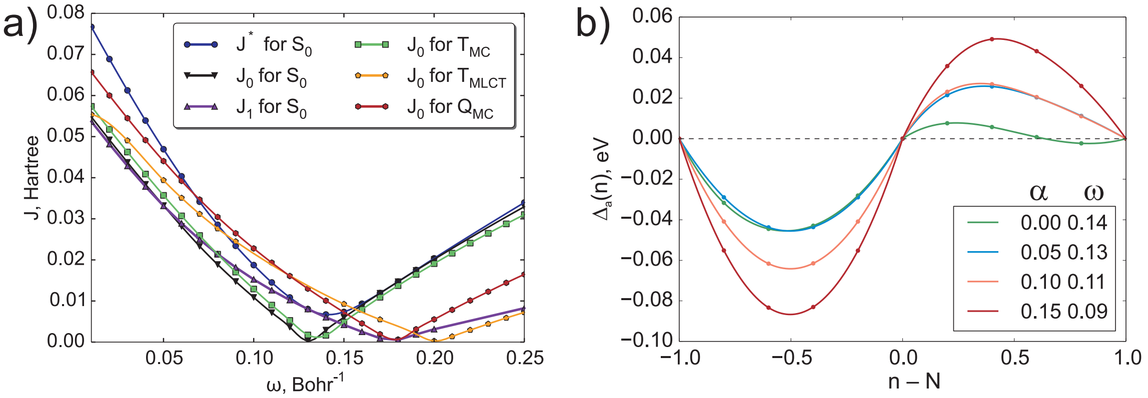

Figure S1: a) Dependencies of $J^*(\alpha, \omega)$ at constant $\alpha$=0. The color code is in accordance with the corresponding 2D-plot in the main text (Figure 2). b) The deviation from the linear dependence $\Delta_a(n)$, see the integrand in eq. S7, for the four best couples of parameters.

the ranges [0.0-0.3] for $\alpha$ and [0.00-0.25] for $\omega$ as being the most reasonable. For tuning of parameters in excited states when ionizing open-shell systems, there is an uncertainty in the choice of the multiplicity of the $N-1$-electron system when computing the IP. Here, we choose to remove an unpaired electron, which leads to the lowering of multiplicity (triplet to doublet and quintet to quartet). The increase of multiplicity has been also analyzed for some cases resulting in generally similar values for both ionization pathways.

Often 2D tuning optimization plots have a distinct valley where the minimal points for a given $\alpha$-value are located[46,60]. For $[Fe(cpmp)_2]^{2+}$in the $S_0$ state, the resulting two-dimensional plot of $J^*(\alpha, \omega)$ is presented by the colored surface in Figure 2 and displays a global minimum of $J^*$ at (0.00; 0.14) located in the valley marked with white circles (for exemplary 1D-cuts at $\alpha$=0, see Fig. S1a).

## S2.2 Piecewise Linearity Criterion

In cases where optimal $(\alpha, \omega)$ pairs correspond to similar $J^*$ values, it is customary to employ an additional criterion for selecting optimal values.[46,60] For example, according to Janak's theorem, the energy $E(N)$ for an exact exchange-correlation functional must vary linearly for fractional electron numbers between integer $N$ values.[61] In reality, this condition is not fulfilled for many functionals pointing to a (de)localization error.[46,62] We have tested the performance of the present parameters along the minimum valley of $J^*(\alpha,\omega)$ in Figure 2 (white line). For all points of $(\alpha;\omega)$ in the valley, we have calculated the deviation of the curvatures of the $E(N)$-dependence for fractional charges from being piecewise linear according to

$$\Delta = \sum_{a=\pm 1} \int_{N+a}^{N} dn \Delta_a(n) = \sum_{a=\pm 1} \int_{N+a}^{N} dn \Big| E(n) - E(N) \\ - \frac{1}{a}[E(N+a) - E(N)](n-N) \Big|. \tag{S7}$$

Thereby $n$ is a non-integer charge of the system, and $a$ can be 1 or $-1$ depending on the situation of adding or removing an electron. The resulting deviations $\Delta_a(n)$ are shown in Figure S1b for four sets of parameters with the smallest deviations from linearity. Note that the deviations from the piecewise linearity of $E(n)$ in Eq. (S7) for the tuned functional are very small, and the values are at least two orders of magnitude smaller than for standard density functionals[63] and, therefore, cannot be considered as an ultimate criterion for choosing optimal range-separation parameters. As can be seen, the global minimum (0.00; 0.14) performs best also in this fractional-electron test. Changing the parameter pair to the next higher $\alpha$ value (0.05; 0.13) gives a similarly good description of the ionized system ($n - N \leq 0$).

## S2.3 Variational Stabilities

An additional criterion for choosing range-separation parameters can be the analysis of variational stabilities of the wave function for neutral and especially ionic species on the ($\alpha$, $\omega$) grid. This criterion can be essential when ionization or explicit redox reactions are considered[60] and also for extended systems, where triplet instability of the ground state may occur.[64–66] However, for $[\mathrm{Fe(cpmp)_2}]^{2+}$, the wave function is variationally stable for all combinations of parameters. Thus, ΔSCF tuning of the $S_0$ state suggests the global minimum of $J^*$ found at (0.00; 0.14) as the optimal range-separation parameters. In the following, it will be abbreviated as Set A. We note, however, that the $J^*$ tuning delivers only a compromise between the $J_0$ (HOMO/IP) and $J_1$ (LUMO/EA) tuning. It can be seen from the black and blue lines in Figure 2, showing the minimal values of $J_0$ and $J_1$ that do not coincide. As both conditions are defined for systems with different number of electrons, the minima should not necessarily be the same.

## S2.4 Triplet Tuning

As an additional option, we have considered the recently suggested "triplet tuning" scheme[56] It is based on the assumption that ΔSCF and TDDFT approaches with the exact exchange-correlation kernel should yield the same energy $E_\mathrm{T}$ of the first triplet excited state. This condition can be achieved by minimizing the following functional $J_\mathrm{TT}$ for tuning:

$$J_\mathrm{TT}(\alpha,\omega) = (E_\mathrm{T}^{\Delta\mathrm{SCF}}(\alpha,\omega) - E_\mathrm{T}^{\mathrm{TDDFT}}(\alpha,\omega))^2 \tag{S8}$$

This approach is not expected to deliver a systematic behavior of $J_\mathrm{TT}$ as it is observed for $J_0$, $J_1$, and $J^*$.[56] Therefore, we will only discuss the position of the global minimum, which is located at (0.10; 0.15), see the yellow star in Figure 2. In general, due to the change of nature (MC vs. MLCT) of the lowest triplet states depending on the range-separation parameters, it is not clear whether a smooth dependency of the tuned functional on the parameters can be expected, as the tuned states may not maintain the same character for the whole range of parameters. In the present case, the optimal parameters obtained with triplet tuning are similar to the $\omega$ value affording a minimum to $J_0$ in the $\mathrm{T}_\mathrm{MLCT}$ state for $\alpha = 0.10$; compare the position of the yellow asterisk and nearest green circle in Figure 2. Fortunately, in this range of parameters, the MLCT state is the lowest one such that the tuning results are consistent with each other.

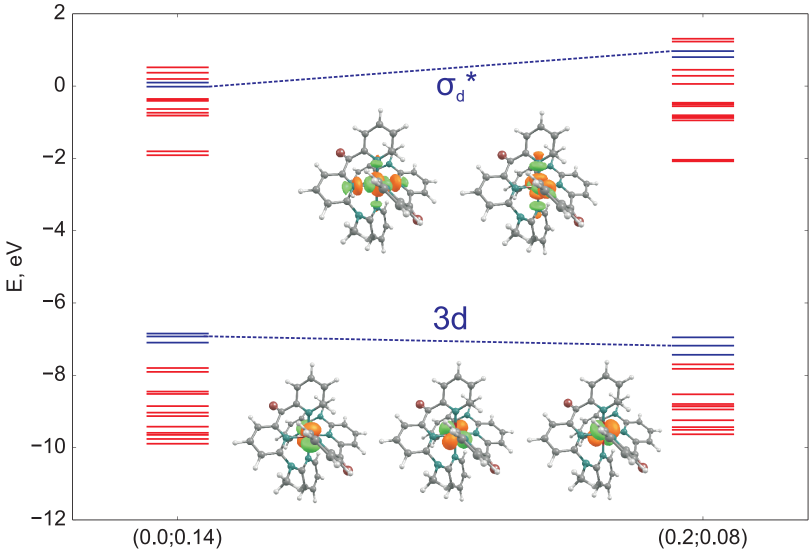

Figure S2: Frontier orbitals of $[Fe(cpmp)_2]^{2+}$computed with Sets A and B of optimal parameters. d and $\sigma$-orbitals (shown as insets) are colored with blue, $\pi$ and $\pi^*$ are marked with red.

## S2.5 Influence of Range-Separation Parameters on Various Properties

Figure S2 presents the orbital diagrams of $[Fe(cpmp)_2]^{2+}$computed with two selected sets of optimal parameters. The orbitals localized on central iron are marked with blue, whereas $\pi$-orbitals of ligands are shown with red. The corresponding $\sigma*$ and 3d-orbitals are shown as insets. Note that visually the localization of orbitals can not be distinguished, but the energies of $\sigma*$ and 3d-orbitals differ notably with the change of the portion of exact exchange in the short range. This observation is additionally supported by the more pronounced MC-character of MC states for larger values of $\alpha$ (see Figure 4 in the main text and Figure S4 below).

The variations of vertical energies of the lowest singlet $S_1$ and triplet $T_1$ states within the studied range of parameters are presented in Figure S3 a) and b). Note that the upper right part of the graph (dashed area) corresponds to the region where the lowest excited state is the MC one.

The Figure S3 (panels c)-e)) demonstrates the adiabatic energies of the two lowest triplet states (of MC and MLCT character) and lowest quintet state (MC character) computed with the whole range of functional parameters. The short version of these three panels is plotted in Figure 3 in the main text, where only the ranges of variations of adiabatic energies of corresponding states are shown against the length of the central Fe-N bond. Note that for the quintet state (panel c)), the values for $\alpha$=0.30 and partially for smaller values (green hatched area) were converged to the false states and excluded from the colormap.

In addition, we have computed the spin-orbit coupling (SOC) matrix elements for the lowest five singlet and triplet states on a 2D $(\alpha, \omega)$ grid. The 2-norms of the respective SOC matrix, $||\mathbf{H}_{\mathrm{SOC}}||_2$, are shown in Fig. S3 f). In general, one can see a systematic increase of SOC with the amount of exact exchange, that is along the diagonal in the $(\alpha, \omega)$ plane. In the range of parameters considered here the magnitude of $||\mathbf{H}_{\mathrm{SOC}}||_2$ changes by a factor of about 2.5 from 1600 to 3700 cm$^{-1}$. To estimate the influence of the $(\alpha, \omega)$ parameters on the state splittings we also computed the 2-norms of the couplings weighted with the energy differences between zero-order states:

$$||\tilde{\mathbf{H}}_{\mathrm{SOC}}||_2 = \sqrt{\sum_{ij} \left( \frac{H_{\mathrm{SOC},ij}}{E_i - E_j} \right)^2} \tag{S9}$$

as their magnitudes are sensitive to the singlet-triplet energetic gaps. These gaps in turn strongly depend on the amount of the exact exchange included in the XC functional that is reflected in the values of SOC elements. The energy-weighted values also vary in quite wide ranges and experience a singularity at the (0.15, 0.10) point since a near exact degeneracy of states is accidentally met. Thus, one can expect the separation parameters to play an important role for theoretical studies of photodynamics if intersystem crossing events are of interest.

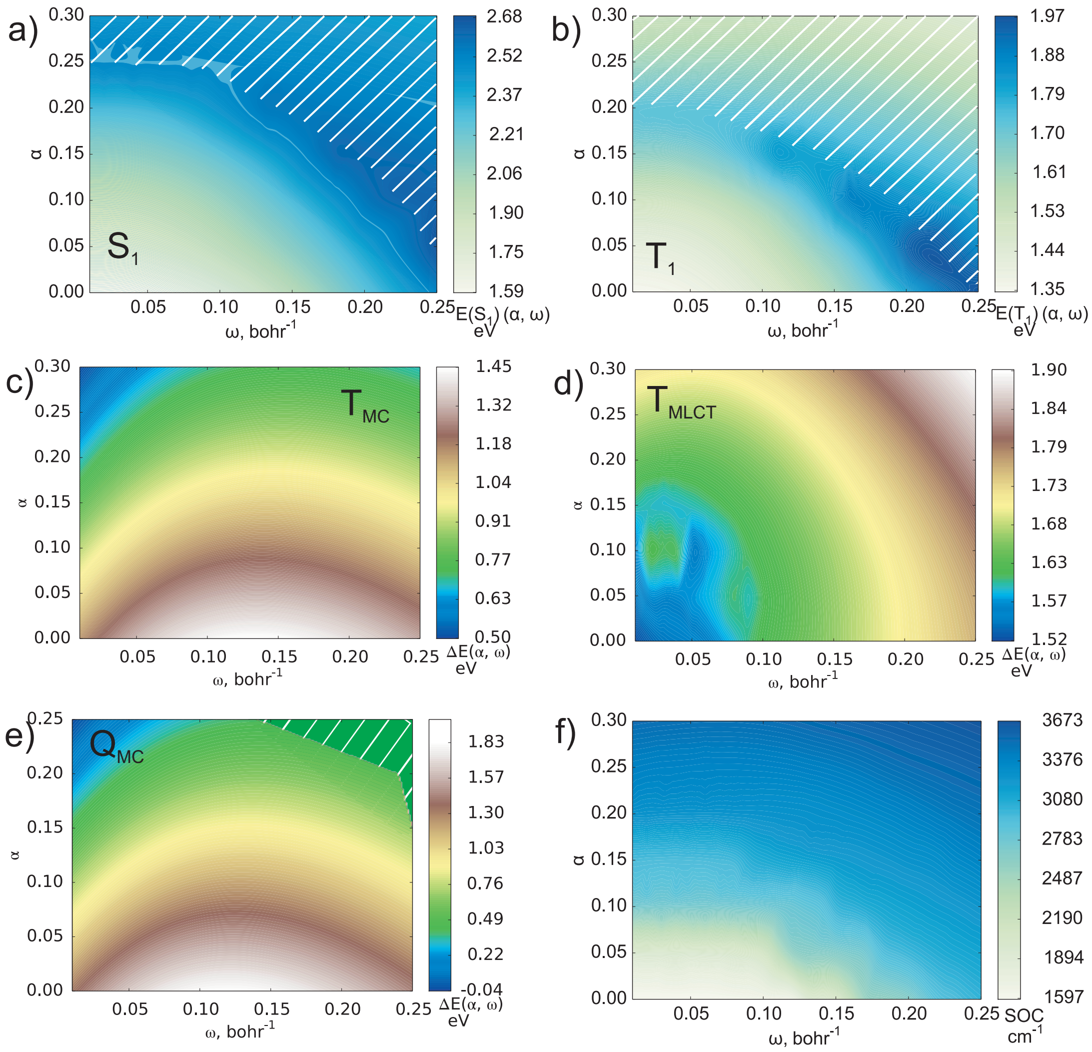

Figure S3: a) and b) Energies of the lowest singlet $S_1$ and triplet $T_1$ vertical excited states as computed with TDDFT on the geometry of the ground state; hatched area marks the ranges of tuning parameters where the lowest singlet state has MC character. Unhatched area corresponds to the MLCT character. c)-e) Adiabatic energies of the $T_{\mathrm{MC}}$, $T_{\mathrm{MLCT}}$, and $Q_{\mathrm{MC}}$ states on the ($\alpha$, $\omega$)-grid. f) 2-norms of the SOC matrix for the 5 singlet and 5 triplet states on the ($\alpha$; $\omega$) grid.

# S3 Influence of basis set and IPEA shift on CASPT2 results

## S3.1 Basis Set Effects

In Figure S4, we show the comparison of the energies of the lowest excited singlet and triplet states of MC and MLCT nature computed with the larger basis set def2TZVP in vacuum (analogously to the results with a smaller basis set 6-31G(d) with PCM solvent in the main text, see Figure 4 and Section 3.3 in the main paper). Note that only the default IPEA shift 0.25 has been applied for CASPT2 in this case.

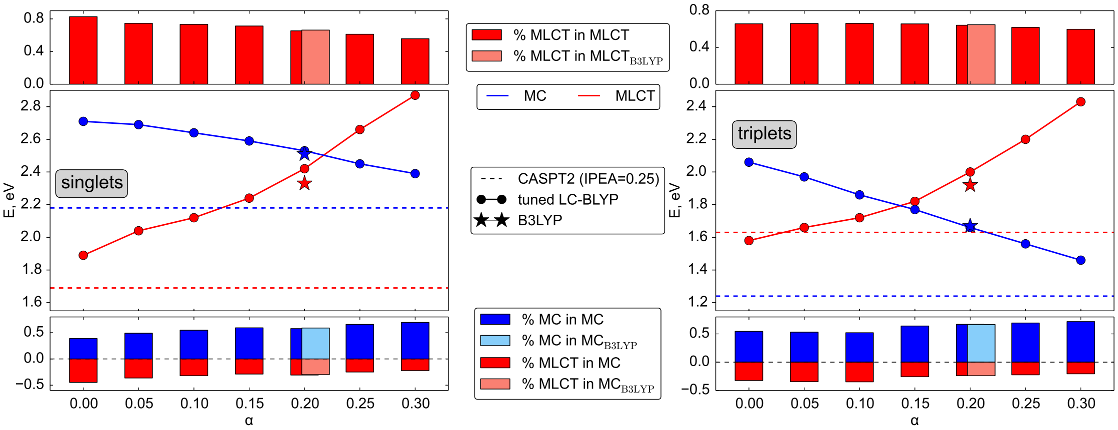

Figure S4: Energies of lowest MC and MLCT states in the singlet (left panel) and triplet (right panel) manifolds predicted by various LC-BLYP variants, as well as B3LYP and CASPT2 reference computed in vacuum with def2TZVP basis set. The percentage of main character of the states is provided in upper (MLCT) and lower (MC) parts of both panels.

## S3.2 IPEA shifts effects

The influence of the IPEA shift[20] on the CASPT2 results has been investigated as well. Introduced to correct for systematic underestimation of open-shell electronic states, the role of the IPEA shift and its recommended value of 0.25 a.u. have been controversial recently.[67] For excitation energies of organic molecules, setting the shift to zero seems beneficial –at least in combination with moderately-sized basis sets.[67] Contrarily, studies on the high-spin-low-spin gaps of hexaaza iron(II) compounds sometimes suggest using even larger IPEA shift values to obtain the correct spin-crossover behavior in CASPT2 calculations.[68–71] Systematic studies on the correct description of excited states of transition-metal complexes – and, in particular, when these states are of different electronic character –however, are still missing. Thus, we have also tested the effect of using a larger IPEA shift value of 0.50 a.u., see Figure 4 in the main paper. For $[\mathrm{Fe(cpmp)_2}]^{2+}$, the usage of IPEA=0.50 a.u. instead of the default parameter 0.25 a.u., led to an overall increase in energies of the lowest excited states, but the MC states were shifted only by about 0.17 eV, whereas the MLCT states are shifted by 0.3–0.4 eV. Comparison of tuned LC-BLYP results with the CASPT2 (IPEA=0.50 a.u.) points again to the (0.20; 0.08) pair (set B), as it provides the best agreement for the order of the lowest singlet and triplet states.

# S4 Nonadiabatic Dynamics

## S4.1 Full Simulation Time

In Figure S5 we present the adiabatic and diabatic state populations for the full simulation time of 2 ps. In the adiabatic state populations, no fits for the kinetic model are shown, since the models discussed in the main paper only included data until 500 fs.

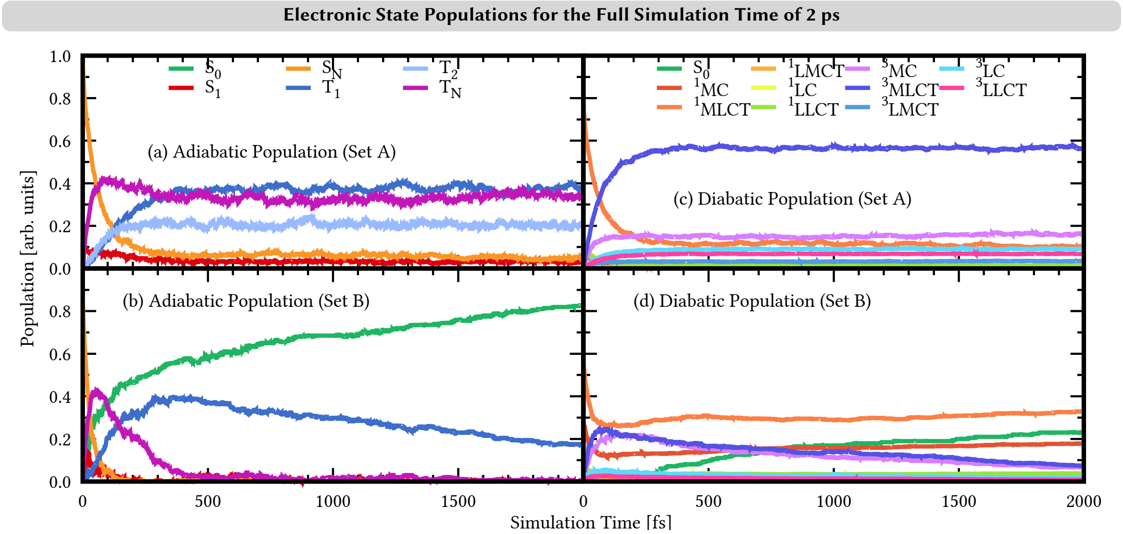

Figure S5: Time evolution of the adiabatic (a/b) and diabatic (c/d) state populations of the LVC/SH dynamics for the complete 2 ps simulation time. (a/c) using range-separation parameters (0.0; 0.14) of set A. (b/d) using range-separation parameters (0.2; 0.08) of set B.

## S4.2 Excited-State Mechanisms

In this section, we explain the derivation of the excited-state mechanisms shown in Figure 7(c,d) in the main paper. For range-separation parameters of set A, excitation in the energy range 1.0-2.5 eV populates initially mostly higher-lying singlet states $S_N$ ($N \geq 2$, 95%, orange line) with some trajectories already starting in the $S_1$ state (5%, red line) as can be seen by the adiabatic state populations in Figure 7(a). The $S_N$ population quickly decreases and falls below 10% within 200 fs. The $S_1$ population first increases to 8% before it steadily decreases to 3% after 500 fs. Within the first few femtoseconds, populations rise in the higher-lying triplet states $T_N$ ($N \geq 3$, violet line), totaling 40% after 100 fs, before they slowly drop to a steady value of 35% after 300 fs. Population starts to accumulate in the lower-lying $T_2$ (light-blue line) and $T_1$ (dark blue line) states after 50 and 100 fs, respectively, which reach a steady state value of 20% and 35% after 300 fs.

The evolution of the adiabatic state population for set A suggests the simple kinetic model

$$\mathrm{S_N} \rightarrow \mathrm{S_1} \rightarrow \mathrm{T_N} \tag{S10}$$

$$\mathrm{S_1} \rightarrow \mathrm{T_N} \tag{S11}$$

$$\mathrm{T_N} \rightarrow \mathrm{T_2} \rightarrow \mathrm{T_1} \tag{S12}$$

Analyzing the hops occurring in the dynamics (Table S1) reveals that the steady population in all three sets of triplet states ($\mathrm{T_N}$, $\mathrm{T_2}$, $\mathrm{T_1}$) is maintained through continuous repopulation of the $\mathrm{T_N}$ from the $\mathrm{T_1}$. Including the pathway

$$\mathrm{T_N} \rightarrow \mathrm{T_1} \tag{S13}$$

in the kinetic model, we show exponential fits in Figure 7(a), while the mechanism including the fitted time constants is summarized in Figure 7(c). As can be seen, the fitted curves (thick lines) closely follow the computed electronic state populations (thin lines), confirming that the simple model of eqs. S10-S13 describes the dynamics well. In this simulation, all major processes, i.e., $\mathrm{S_N}\rightarrow\mathrm{T_N}$ intersystem crossing as well as $\mathrm{T_N}\rightarrow\mathrm{T_2}$ and $\mathrm{T_2}\rightarrow\mathrm{T_1}$ internal conversion, occur on sub-100 fs time scales.

In Figure 7(b) we show the time evolution of the adiabatic state populations from simulations on LVC potentials using the range-separation parameters of set B. Again, most trajectories are started in higher-lying singlet states $\mathrm{S_N}$ (85%), although now a larger portion is initiated in the $\mathrm{S_1}$ state (15%). Both sets of singlet populations readily decrease to 1-2% within 100 fs. Within few femtoseconds, populations starts to accumulate in both, the higher-lying triplet states $\mathrm{T_N}$ –where we have now included the $\mathrm{T_2}$ state – and the singlet ground state $\mathrm{S_0}$. With some delay, population also increases in the $\mathrm{T_1}$ state. The $\mathrm{T_N}$ population reaches a maximum of 40% at 50 fs and decreases to 4% after 500 fs. The $\mathrm{T_1}$ population increases to 35% at 300 fs before it slowly decreases, reaching 20% after 2 ps (see Figure S5 in the SI). The fast initial increase of the $\mathrm{S_0}$ populations slows down after 100 fs, however the $S_0$ population continues to rise, reaching 60% after 500 fs and 80% after 2 ps.

The evolution of the adiabatic state population for set B suggests the simple kinetic model

$$\mathrm{S_N \rightarrow S_1 \rightarrow S_0} \tag{S14}$$

$$\mathrm{S_N \rightarrow T_N \rightarrow T_1 \rightarrow S_0} \tag{S15}$$

Exponential fits (thick lines) shown in Figure 7(b) for this mechanism again closely follow the simulated electronic state populations (thin lines), confirming that eqs S14 and S15 adequately describe the simulated dynamics. Time constants for the fits are shown in Figure 7(d).

As can be seen, population from the $S_N$ is split in sub-100 fs reactions with the majority undergoing intersystem crossing into the $T_N$ states and a smaller portion undergoing internal conversion to the $S_1$ state. From the $S_1$ state, all population relaxes to the $S_0$ ground state on a 20 fs time scale. The population in the higher-lying triplet states $T_N$ is transferred to the $T_1$ state on a 150 fs time scale, before the population in the triplet manifold relaxes back to the $S_0$. This triplet-to-singlet back intersystem crossing occurs on a 750 fs time scale, accounting for the slower component in the rise of the $S_0$ population.

## S4.3 Hops During the Dynamics

In Tables S1 and S2 we report the difference number of hops from the linear-vibronic coupling/surface hopping (LVC/SH) simulations based on the LC-BLYP potenitals using set A and set B, respectively. The hops are counted for 1000 trajectories each propagated for 4000 time steps of 0.5 fs. The difference number of hops counts only the net number of hops in a specific direction (from one state to another state), i.e., hops in the reverse direction cancel out.

Table S1: Difference number in hops from singlet to singlet/triplet adiabatic states from the LVC/SH dynamics using longe-range parameters of set A. Continued next page.

| | $S_0$ | $S_1$ | $S_2$ | $S_3$ | $S_4$ | $S_5$ | $S_6$ | $S_7$ | $S_8$ | $S_9$ | $S_{10}$ |
|---|---|---|---|---|---|---|---|---|---|---|---|
| $S_0$ | 0 | 0 | 0 | 0 | 0 | 0 | 0 | 0 | 0 | 0 | 0 |
| $S_1$ | 0 | 0 | 59 | -88 | -16 | 2 | 0 | -1 | 0 | -2 | -3 |
| $S_2$ | 0 | -59 | 0 | 423 | 49 | -11 | -11 | 0 | -1 | 0 | 0 |
| $S_3$ | 0 | 88 | -423 | 0 | 161 | 27 | 4 | -1 | -1 | -2 | -1 |
| $S_4$ | 0 | 16 | -49 | -161 | 0 | -1 | 18 | -3 | 1 | -1 | 0 |
| $S_5$ | 0 | -2 | 11 | -27 | 1 | 0 | -30 | -2 | -2 | -2 | 0 |
| $S_6$ | 0 | 0 | 11 | -4 | -18 | 30 | 0 | 53 | -4 | 0 | 0 |
| $S_7$ | 0 | 1 | 0 | 1 | 3 | 2 | -53 | 0 | 42 | -2 | 1 |
| $S_8$ | 0 | 0 | 1 | 1 | -1 | 2 | 4 | -42 | 0 | 26 | -2 |
| $S_9$ | 0 | 2 | 0 | 2 | 1 | 2 | 0 | 2 | -26 | 0 | 3 |
| $S_{10}$ | 0 | 3 | 0 | 1 | 0 | 0 | 0 | -1 | 2 | -3 | 0 |
| $T_1$ | 0 | -20 | -2 | -2 | 1 | 0 | 1 | 0 | 0 | -1 | 0 |
| $T_2$ | 0 | -31 | -8 | -2 | 2 | 0 | -1 | -2 | 0 | 0 | 0 |
| $T_3$ | 0 | 108 | 24 | -6 | 0 | -1 | -1 | 0 | 0 | -2 | -1 |
| $T_4$ | 0 | 42 | 125 | -16 | -7 | -1 | -2 | 0 | 0 | 0 | -1 |
| $T_5$ | 0 | -14 | 215 | -47 | -11 | 3 | -1 | 0 | 0 | 0 | 0 |
| $T_6$ | 0 | -59 | 179 | 194 | -21 | -10 | -2 | 0 | 0 | -1 | -1 |
| $T_7$ | 0 | -45 | -10 | 1 | 66 | 65 | -4 | 0 | -1 | 0 | 0 |
| $T_8$ | 0 | -14 | -44 | 2 | 21 | 82 | 11 | -2 | 0 | 0 | 0 |
| $T_9$ | 0 | -2 | -26 | -28 | 13 | 39 | 11 | -1 | 0 | 0 | 0 |
| $T_{10}$ | 0 | 3 | -1 | -3 | -26 | 22 | 64 | 7 | 1 | -1 | 0 |
| $T_{11}$ | 0 | -1 | 0 | -18 | 7 | 13 | 57 | 8 | -1 | 0 | 0 |
| $T_{12}$ | 0 | 0 | 2 | -5 | -12 | 3 | 35 | 5 | 7 | 0 | 0 |
| $T_{13}$ | 0 | 0 | 1 | 1 | 0 | 0 | 4 | 11 | 4 | -3 | 0 |
| $T_{14}$ | 0 | 0 | 0 | 1 | -1 | 0 | 0 | -7 | -16 | 9 | 2 |
| $T_{15}$ | 0 | 0 | 0 | 1 | 0 | 0 | 1 | -9 | -3 | -7 | 0 |
| $T_{16}$ | 0 | 2 | 1 | 0 | 0 | 0 | 0 | -5 | -1 | 6 | -2 |
| $T_{17}$ | 0 | 0 | 2 | 0 | 0 | 0 | 0 | -6 | 0 | -14 | 3 |
| $T_{18}$ | 0 | 3 | 0 | 1 | 0 | 0 | 0 | 1 | -4 | 3 | 4 |
| $T_{19}$ | 0 | 1 | 0 | 0 | 0 | 0 | 0 | 1 | 6 | -5 | 1 |
| $T_{20}$ | 0 | 0 | 0 | 0 | 0 | 0 | 0 | -1 | -2 | 1 | -3 |
| Sum | 0 | 22 | 68 | 222 | 212 | 268 | 105 | 5 | 1 | -1 | 0 |

| | $T_1$ | $T_2$ | $T_3$ | $T_4$ | $T_5$ | $T_6$ | $T_7$ | $T_8$ | $T_9$ | $T_{10}$ | $T_{11}$ | $T_{12}$ | $T_{13}$ | $T_{14}$ | $T_{15}$ | $T_{16}$ | $T_{17}$ | $T_{18}$ | $T_{19}$ | $T_{20}$ | Sum |
|---|---|---|---|---|---|---|---|---|---|---|---|---|---|---|---|---|---|---|---|---|---|
| $S_0$ | 0 | 0 | 0 | 0 | 0 | 0 | 0 | 0 | 0 | 0 | 0 | 0 | 0 | 0 | 0 | 0 | 0 | 0 | 0 | 0 | 0 |
| $S_1$ | 20 | 31 | -108 | -42 | 14 | 59 | 45 | 14 | 2 | -3 | 1 | 0 | 0 | 0 | 0 | -2 | 0 | -3 | -1 | 0 | -22 |
| $S_2$ | 2 | 8 | -24 | -125 | -215 | -179 | 10 | 44 | 26 | 1 | 0 | -2 | -1 | 0 | 0 | -1 | -2 | 0 | 0 | 0 | -68 |
| $S_3$ | 2 | 2 | 6 | 16 | 47 | -194 | -1 | -2 | 28 | 3 | 18 | 5 | -1 | -1 | -1 | 0 | 0 | -1 | 0 | 0 | -222 |
| $S_4$ | -1 | -2 | 0 | 7 | 11 | 21 | -66 | -21 | -13 | 26 | -7 | 12 | 0 | 1 | 0 | 0 | 0 | 0 | 0 | 0 | -212 |
| $S_5$ | 0 | 0 | 1 | 1 | -3 | 10 | -65 | -82 | -39 | -22 | -13 | -3 | 0 | 0 | 0 | 0 | 0 | 0 | 0 | 0 | -268 |
| $S_6$ | -1 | 1 | 1 | 2 | 1 | 2 | 4 | -11 | -11 | -64 | -57 | -35 | -4 | 0 | -1 | 0 | 0 | 0 | 0 | 0 | -105 |
| $S_7$ | 0 | 2 | 0 | 0 | 0 | 0 | 0 | 2 | 1 | -7 | -8 | -5 | -11 | 7 | 9 | 5 | 6 | -1 | -1 | 1 | -5 |
| $S_8$ | 0 | 0 | 0 | 0 | 0 | 0 | 1 | 0 | 0 | -1 | 1 | -7 | -4 | 16 | 3 | 1 | 0 | 4 | -6 | 2 | -1 |
| $S_9$ | 1 | 0 | 2 | 0 | 0 | 1 | 0 | 0 | 0 | 1 | 0 | 0 | 3 | -9 | 7 | -6 | 14 | -3 | 5 | -1 | 1 |
| $S_{10}$ | 0 | 0 | 1 | 1 | 0 | 1 | 0 | 0 | 0 | 0 | 0 | 0 | 0 | -2 | 0 | 2 | -3 | -4 | -1 | 3 | 0 |
| $T_1$ | 0 | 1050 | -358 | -41 | -38 | -13 | -29 | -17 | -9 | -19 | -17 | -9 | -14 | -18 | -23 | -15 | -13 | -3 | -8 | -8 | 375 |
| $T_2$ | -1050 | 0 | 1922 | -297 | -138 | -61 | -26 | 4 | -19 | -11 | -11 | -9 | -4 | -11 | -9 | -10 | -16 | -2 | -2 | -4 | 204 |
| $T_3$ | 358 | -1922 | 0 | 1695 | -30 | -9 | -27 | 2 | -12 | -3 | -10 | -10 | -5 | -5 | -6 | -4 | -8 | -5 | -8 | -7 | 105 |
| $T_4$ | 41 | 297 | -1695 | 0 | 1186 | 185 | -43 | 0 | -9 | -8 | -9 | 3 | -4 | -6 | -2 | -5 | -3 | -5 | -1 | -1 | 61 |
| $T_5$ | 38 | 138 | 30 | -1186 | 0 | 951 | -43 | 4 | -13 | 2 | -3 | -4 | -2 | -2 | -5 | -2 | -4 | -3 | -2 | -1 | 38 |
| $T_6$ | 13 | 61 | 9 | -185 | -951 | 0 | 765 | 87 | -7 | -7 | 0 | -1 | -3 | -1 | -3 | -3 | -2 | -2 | -2 | 0 | 47 |
| $T_7$ | 29 | 26 | 27 | 43 | 43 | -765 | 0 | 499 | 35 | 18 | 7 | 0 | -2 | -2 | -2 | -1 | -3 | -1 | -2 | -2 | 19 |
| $T_8$ | 17 | -4 | -2 | 0 | -4 | -87 | -499 | 0 | 440 | 68 | 21 | 7 | -2 | 1 | 0 | 1 | -1 | 0 | -1 | -1 | 10 |
| $T_9$ | 9 | 19 | 12 | 9 | 13 | 7 | -35 | -440 | 0 | 353 | 45 | 22 | -2 | 3 | 0 | -1 | -2 | 0 | -2 | 0 | 16 |
| $T_{10}$ | 19 | 11 | 3 | 8 | -2 | 7 | -18 | -68 | -353 | 0 | 298 | 39 | -3 | 1 | -3 | 1 | 0 | 0 | 0 | 0 | 6 |
| $T_{11}$ | 17 | 11 | 10 | 9 | 3 | 0 | -7 | -21 | -45 | -298 | 0 | 248 | 14 | 1 | 1 | 0 | 1 | -2 | -1 | 0 | 6 |
| $T_{12}$ | 9 | 9 | 10 | -3 | 4 | 1 | 0 | -7 | -22 | -39 | -248 | 0 | 247 | 9 | -4 | 2 | -2 | 2 | 0 | 1 | 4 |
| $T_{13}$ | 14 | 4 | 5 | 4 | 2 | 3 | 2 | 2 | 2 | 3 | -14 | -247 | 0 | 179 | 21 | -1 | 1 | 5 | 1 | -1 | 3 |
| $T_{14}$ | 18 | 11 | 5 | 6 | 2 | 1 | 2 | -1 | -3 | -1 | -1 | -9 | -179 | 0 | 119 | 25 | 8 | 4 | 3 | 3 | 1 |
| $T_{15}$ | 23 | 9 | 6 | 2 | 5 | 3 | 2 | 0 | 0 | 3 | -1 | 4 | -21 | -119 | 0 | 104 | 0 | 2 | -2 | -1 | 2 |
| $T_{16}$ | 15 | 10 | 4 | 5 | 2 | 3 | 1 | -1 | 1 | -1 | 0 | -2 | 1 | -25 | -104 | 0 | 59 | 26 | 5 | 0 | 0 |
| $T_{17}$ | 13 | 16 | 8 | 3 | 4 | 2 | 3 | 1 | 2 | 0 | -1 | 2 | -1 | -8 | 0 | -59 | 0 | 22 | 0 | 9 | 1 |
| $T_{18}$ | 3 | 2 | 5 | 5 | 3 | 2 | 1 | 0 | 0 | 0 | 2 | -2 | -5 | -4 | -2 | -26 | -22 | 0 | 28 | 4 | 2 |
| $T_{19}$ | 8 | 2 | 8 | 1 | 2 | 2 | 2 | 1 | 2 | 0 | 1 | 0 | -1 | -3 | 2 | -5 | 0 | -28 | 0 | 2 | 0 |
| $T_{20}$ | 8 | 4 | 7 | 1 | 1 | 0 | 2 | 1 | 0 | 0 | 0 | -1 | 1 | -3 | 1 | 0 | -9 | -4 | -2 | 0 | 2 |
| Sum | -375 | -204 | -105 | -61 | -38 | -47 | -19 | -10 | -16 | -6 | -6 | -4 | -3 | -1 | -2 | 0 | -1 | -2 | 0 | -2 | 0 |

Table S1: (Continued) Difference number in hops from triplet to singlet/triplet adiabatic states from the LVC/SH dynamics using longe-range parameters of set A.

|  | $S_0$ | $S_1$ | $S_2$ | $S_3$ | $S_4$ | $S_5$ | $S_6$ | $S_7$ | $S_8$ | $T_1$ | $T_2$ | $T_3$ | $T_4$ | $T_5$ | $T_6$ | $T_7$ | $T_8$ | $T_9$ | $T_{10}$ | $T_{11}$ | $T_{12}$ | $T_{13}$ | $T_{14}$ | Sum |
|---|---|---|---|---|---|---|---|---|---|---|---|---|---|---|---|---|---|---|---|---|---|---|---|---|
| $S_0$ | 0 | 432 | 3 | -3 | 0 | 0 | 0 | 0 | 0 | 363 | 22 | 0 | 0 | 0 | 0 | 0 | 0 | 0 | 0 | 0 | 0 | 0 | 0 | 817 |
| $S_1$ | -432 | 0 | 260 | 12 | 12 | 2 | -1 | -1 | -2 | -2 | -4 | -19 | 2 | -12 | 11 | -10 | -11 | -5 | 2 | -3 | -2 | -1 | 0 | -204 |
| $S_2$ | -3 | -260 | 0 | 107 | 11 | 0 | 0 | 0 | 0 | -15 | -18 | 2 | -9 | -21 | -23 | 3 | -25 | -32 | 1 | 0 | 10 | 1 | 0 | -271 |
| $S_3$ | 3 | -12 | -107 | 0 | 83 | -6 | -6 | 1 | 2 | 0 | -2 | -4 | -9 | -11 | -21 | -29 | -36 | -23 | -40 | -9 | -18 | 1 | 0 | -243 |
| $S_4$ | 0 | -12 | -11 | -83 | 0 | 51 | -4 | 1 | -5 | 0 | 0 | 1 | 1 | -1 | -2 | -6 | -13 | -20 | -29 | -40 | -5 | -4 | 0 | -181 |
| $S_5$ | 0 | -2 | 0 | 6 | -51 | 0 | 39 | -7 | 0 | 0 | 0 | 0 | 0 | 0 | -1 | 0 | -1 | -7 | -8 | -8 | -22 | -7 | 1 | -68 |
| $S_6$ | 0 | 1 | 0 | 6 | 4 | -39 | 0 | 18 | -3 | 0 | 0 | 0 | 0 | 0 | 1 | 0 | 1 | -1 | -1 | -1 | -11 | 4 | -2 | -23 |
| $S_7$ | 0 | 1 | 0 | -1 | -1 | 7 | -18 | 0 | 6 | 0 | 0 | 0 | 0 | 0 | 0 | 0 | -1 | -1 | 2 | -3 | 4 | 1 | -1 | -5 |
| $S_8$ | 0 | 2 | 0 | -2 | 5 | 0 | 3 | -6 | 0 | 0 | 0 | 0 | 0 | 0 | 0 | 0 | 0 | 0 | 0 | 1 | -1 | -1 | -1 | 0 |
| $T_1$ | -363 | 2 | 15 | 0 | 0 | 0 | 0 | 0 | 0 | 0 | 504 | 38 | -6 | -4 | -5 | -1 | 0 | -1 | -1 | -1 | 0 | -1 | 0 | 176 |
| $T_2$ | -22 | 4 | 18 | 2 | 0 | 0 | 0 | 0 | 0 | -504 | 0 | 421 | 63 | 9 | 13 | 2 | 0 | 2 | 2 | -3 | -3 | 0 | 0 | 4 |
| $T_3$ | 0 | 19 | -2 | 4 | -1 | 0 | 0 | 0 | 0 | -38 | -421 | 0 | 333 | 68 | 18 | 14 | 4 | 1 | 2 | 1 | 0 | 0 | -1 | 1 |
| $T_4$ | 0 | -2 | 9 | 9 | -1 | 0 | 0 | 0 | 0 | 6 | -63 | -333 | 0 | 323 | 27 | 6 | 15 | 0 | 4 | 1 | 2 | -2 | -1 | 0 |
| $T_5$ | 0 | 12 | 21 | 11 | 1 | 0 | 0 | 0 | 0 | 4 | -9 | -68 | -323 | 0 | 270 | 51 | 17 | 9 | 3 | 5 | -3 | 0 | -1 | 0 |
| $T_6$ | 0 | -11 | 23 | 21 | 2 | 1 | -1 | 0 | 0 | 5 | -13 | -18 | -27 | -270 | 0 | 261 | 34 | 3 | -2 | -4 | -6 | 1 | 1 | 0 |
| $T_7$ | 0 | 10 | -3 | 29 | 6 | 0 | 0 | 0 | 0 | 1 | -2 | -14 | -6 | -51 | -261 | 0 | 227 | 47 | 5 | 8 | 3 | 1 | 0 | 0 |
| $T_8$ | 0 | 11 | 25 | 36 | 13 | 1 | -1 | 1 | 0 | 0 | 0 | -4 | -15 | -17 | -34 | -227 | 0 | 150 | 38 | 25 | 1 | -2 | 0 | 1 |
| $T_9$ | 0 | 5 | 32 | 23 | 20 | 7 | 1 | 1 | 0 | 1 | -2 | -1 | 0 | -9 | -3 | -47 | -150 | 0 | 97 | 31 | -4 | -1 | -1 | 0 |
| $T_{10}$ | 0 | -2 | -1 | 40 | 29 | 8 | 1 | -2 | 0 | 1 | -2 | -2 | -4 | -3 | 2 | -5 | -38 | -97 | 0 | 53 | 14 | 5 | 0 | -3 |
| $T_{11}$ | 0 | 3 | 0 | 9 | 40 | 8 | 1 | 3 | -1 | 1 | 3 | -1 | -1 | -5 | 4 | -8 | -25 | -31 | -53 | 0 | 49 | 5 | -2 | -1 |
| $T_{12}$ | 0 | 2 | -10 | 18 | 5 | 22 | 11 | -4 | 1 | 0 | 3 | 0 | -2 | 3 | 6 | -3 | -1 | 4 | -14 | -49 | 0 | 6 | 2 | 0 |
| $T_{13}$ | 0 | 1 | -1 | -1 | 4 | 7 | -4 | -1 | 1 | 1 | 0 | 0 | 2 | 0 | -1 | -1 | 2 | 1 | -5 | -5 | -6 | 0 | 6 | 0 |
| $T_{14}$ | 0 | 0 | 0 | 0 | 0 | -1 | 2 | 1 | 1 | 0 | 0 | 1 | 1 | 1 | -1 | 0 | 0 | 1 | 0 | 2 | -2 | -6 | 0 | 0 |
| Sum | -817 | 204 | 271 | 243 | 181 | 68 | 23 | 5 | 0 | -176 | -4 | -1 | 0 | 0 | 0 | 0 | -1 | 0 | 3 | 1 | 0 | 0 | 0 | 0 |

Table S2: Difference number in hops between singlet and triplet adiabatic states from the LVC/SH dynamics using longe-range parameters of set B.

## S4.4 Diabatic Character of the Trajectories

### S4.4.1 Discussion of the Mechanisms

In the main paper, we state that the admixture of $^3$MLCT and $^3$MC character in the diabatic state population in the set A dynamics is due to state mixing rather than the system traversing two different pathways. In order to demonstrate this, we show the time evolution of the dominant diabatic contribution to the electronic state of a random selection of 50 trajectories in the dynamics shown in Figure S6(a). A contribution is considered dominant if its weight $|c|^2$ in the electronic wave function is at least 50%. Results applying a stricter threshold are discussed in Section S4.5. As can be seen in Figure S6(a), the trajectories are dominated most of the simulation time by the $^3$MLCT character (dark blue). Occasionally, the dominant character changes to $^3$MC (violet), but always for short intervals before it switches back to $^3$MLCT. If a minor pathway populating $^3$MC states existed, the analysis in Figure S6(a) would display a small number of trajectories with dominant $^3$MC character in place of these oscillations. Similarly to the $^3$MLCT/$^3$MC oscillations, some trajectories display back-and-forth switching between $^3$MLCT and $^1$MLCT character (orange).

The difference between the adiabatic and diabatic $S_0$ populations in the set B dynamics can be explained when analyzing the dominant diabatic state characters of the trajectories. As can be seen in Figure S6(b), a number of trajectories exhibit dominant diabatic $S_0$ character (green). These trajectories enter $S_0$ characters mainly from the $^3$MC character (violet). More examples of this behavior are shown in the full dynamics of Figure S8. Thus, the diabatic $S_0$ only seems to be readily reached via the triplet states according to eq. S15. In the other relaxation pathways to the adiabatic $S_0$ state, the trajectories still possess large portions of $^1$MLCT character as is also displayed by the many dominant $^1$MLCT contributions (orange) in Figure S6(b).

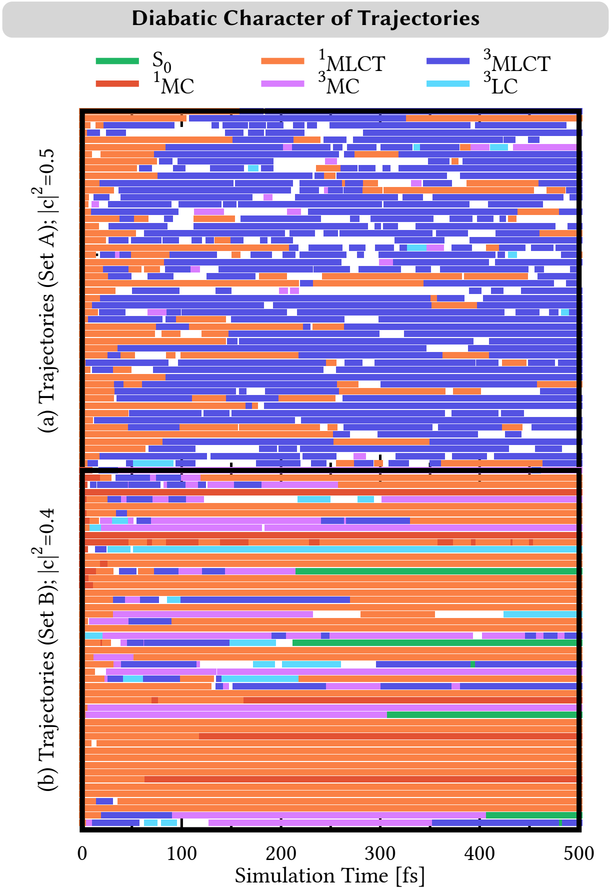

Figure S6: Time evolution of the dominant diabatic contribution to the electronic state of a random selection of 50 trajectories for dynamics using range-separation parameters set A and set B in (a) and (b), respectively. Dominant contributions above thresholds of $|c|^2 = 0.5$ (a) and $|c|^2 = 0.4$ (b). Blank areas denote simulation times without a dominant state according to the $|c|^2$ threshold criterion.

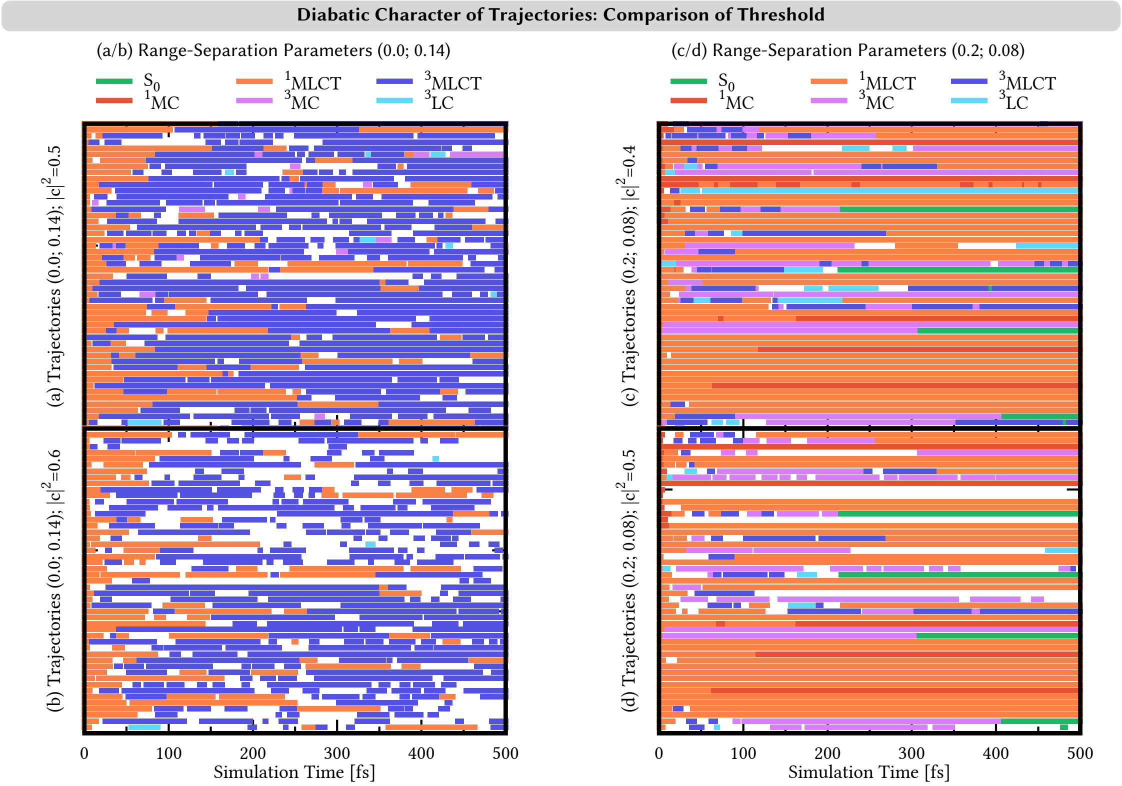

Figure S7: Comparison of threshold $|c|^2$ for assigning trajectories to a dominant diabatic state characters for dynamics using set A in (a/b) and set B in (c/d), respectively.

## S4.5 Threshold of Classification

For range-separation parameters set A and set B, we thereby used threshold of $|c|^2 = 0.5$ and $|c|^2 = 0.4$, respectively, in order to classify a state character as dominant. Here, in Figure S7, we compare this analysis with one using stricter thresholds, i.e., $|c|^2 = 0.6$ and $|c|^2 = 0.5$ for set A and set B, respectively. As can be seen in Figure S7(a/b) for set A, increasing the threshold from 50% to 60% affects mainly the assignment of trajectories to $^3$MLCT states (dark blue). This difference is simply due to these trajectories possessing $^3$MLCT characters between 50-60%.

Using set B, comparing the thresholds 40% and 50% shows little difference for most trajectories, that are in diabatic $^1$MLCT states. Differences are mostly seen for trajectories in triplet states, signifying a stronger mixing of state character.

In addition, we show the diabatic character of the trajectories for the full simulation time

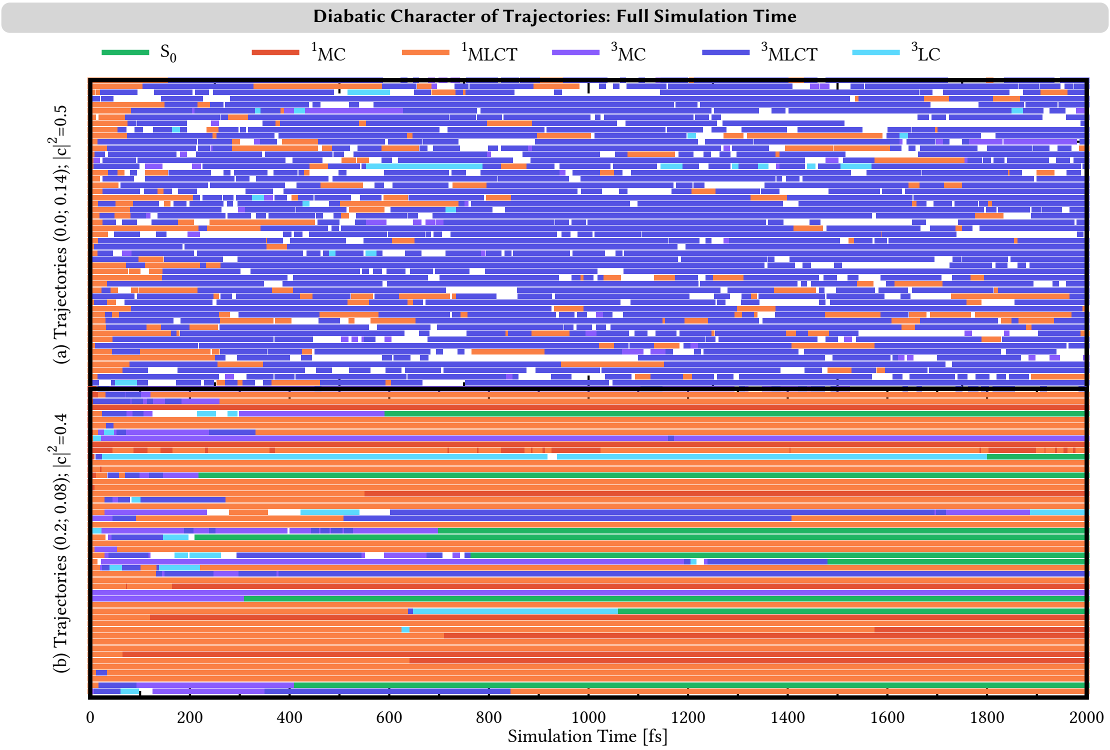

Figure S8: Diabatic character of the trajectories for the full simulation time of 2 ps.

of 2 ps using the thresholds of 0.5 and 0.3 for set A and set B, respectively, in Figure S8.

## S4.6 Example Trajectories Shown for Extended Simulation Times

The difference between the adiabatic and diabatic $S_0$ populations can be understood by investigating the behavior of trajectories undergoing deactivation within the singlet manifold in more detail. To do this, we show the potentials of the singlet (blue lines) and triplet (red lines) electronic states along example trajectories in Figure S9, where the active electronic is marked by black circles. Figure S9(a) shows the ultrafast relaxation of a trajectory within the singlet manifold from the initial excited singlet state to the adiabatic ground state within 22 fs. Analyzing the diabatic character of this state reveals predominant $^1$MLCT and $^1$MC characters. This state is still close in energy to the excited singlet and triplet states, indicating that it is still displaced from the Franck-Condon geometry (where adiabatic and diabatic $S_0$ states coincide). Thus, this state is denoted as $S_0^*$ and can be viewed as a hot

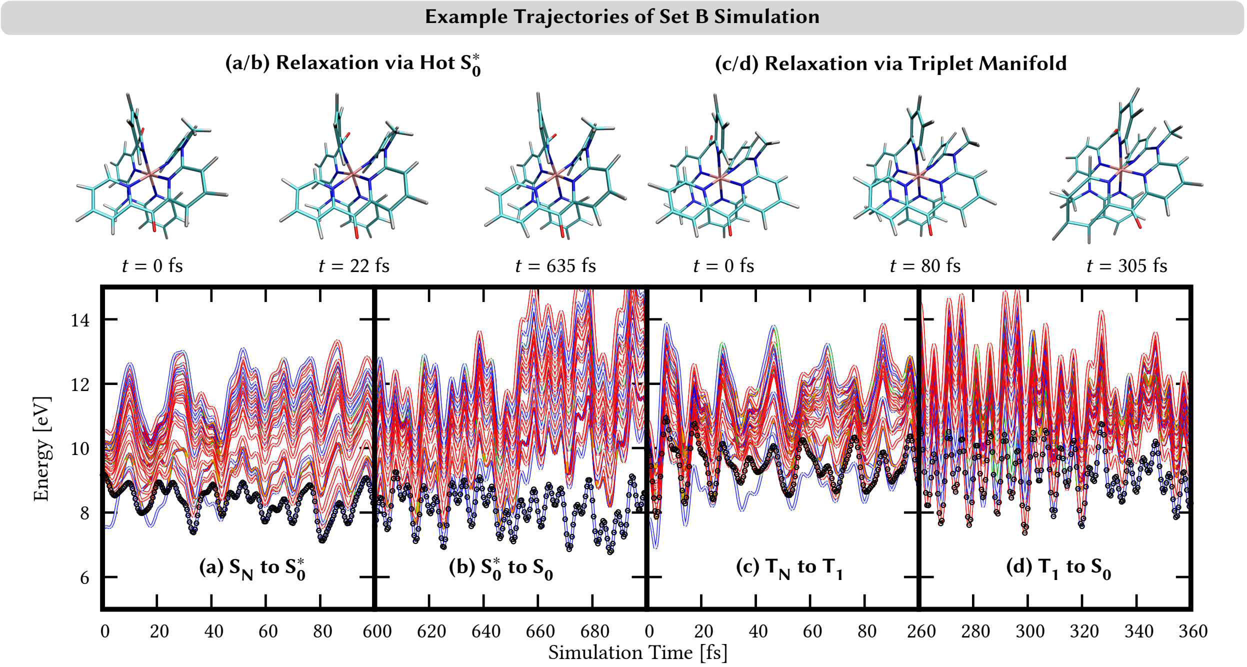

Figure S9: Example trajectories from LVC/SH simulations using range-separation parameters of set B. Selected simulation windows from a trajectory relaxing via the hot $S_0^*$ state (a/b) or relaxing via the triplet manifold (c/d). Lines depict electronic potentials of all states during the simulation. Black circles denote the active state during the simulation. Line color refers to spin expectation value $\langle S^2 \rangle$ of the electronic states: 0 (blue), 1 (green), 2 (red). Top panel: geometries from the beginning of the dynamics and at the transition between the $S_0^*/S_0$ and $T_1/S_0$ states.

ground state. The $S_0^*$ is maintained in the trajectory until ca. 635 fs, where the dominant character changes to the diabatic $S_0$ and the state is separated in energy from the excited singlet and triplet states; see Figure S9(b). The full simulation of 0-1000 fs of this trajectory is also shown in Figure S10.

For comparison, we show in Figure S9(c/d) a trajectory that traverses via the triplet pathway, first relaxing to the adiabatic $T_1$ state (80 fs) before it reaches the ground state $S_0$. In this case, i.e., when reaching the adiabatic $S_0$ state from the triplet manifold, the state takes immediately a diabatic $S_0$ character and separates in energy from the other electronic states. Before re-entering the singlet manifold, however, also the triplet-pathway trajectory passes through geometries with many low-lying electronic states close in energy. Selected representative geometries of both trajectories are also depicted in Figure S9.

**(a) Extended Example Trajectories of Set B Simulation: Relaxation via Hot $S_0^*$**

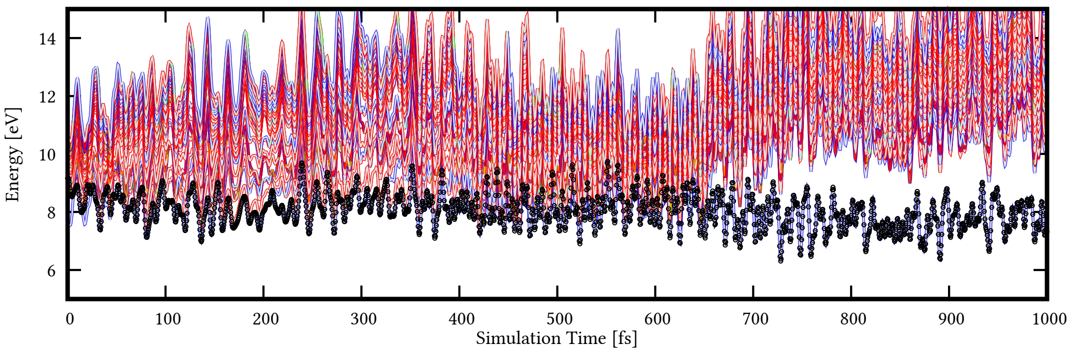

**(b) Extended Example Trajectories of Set B Simulation: Relaxation via Triplet Manifold**

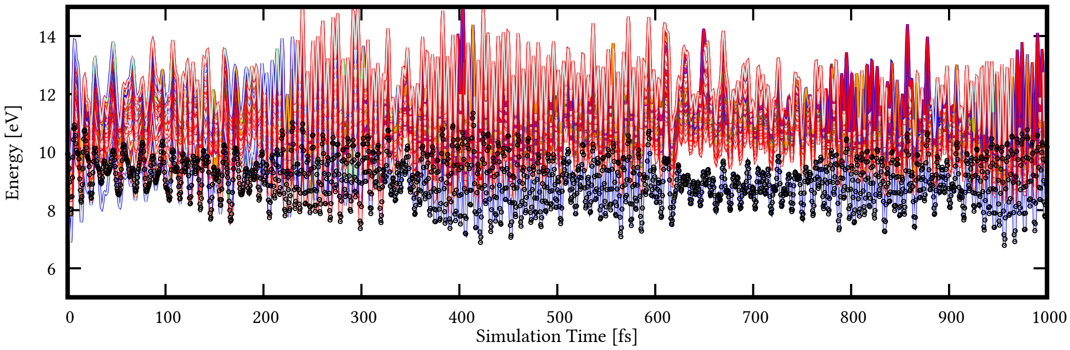

Figure S10: Example trajectories from LVC/SH simulations using range-separation parameters of set B. Simulation from a trajectory relaxing via the hot $S_0^*$ state (a) or relaxing via the triplet manifold (b). Lines depict electronic potentials of all states during the simulation. Black circles denote the active state during the simulation. Line color refers to spin expectation value of the electronic states: 0 (blue), 1 (green), 2 (red).

## S4.7 Rationalizing the Simulated Mechanisms based on the Density of States at the Franck-Condon Geometry

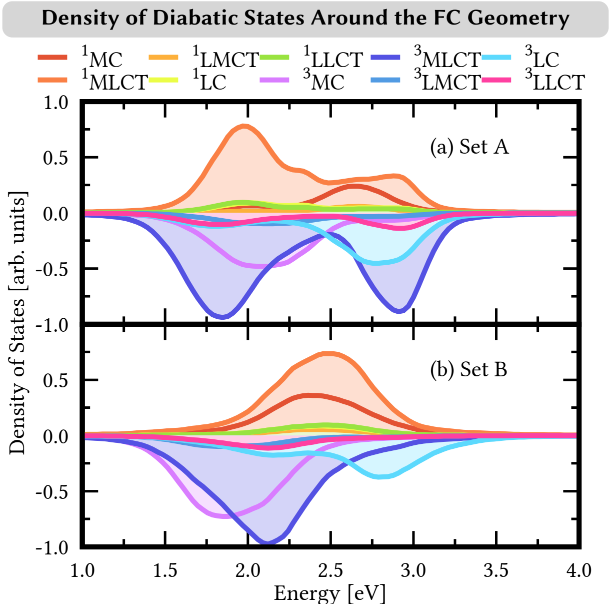

Figure S11: Density of diabatic singlet states (positive axis) and triplet states (negative axis) of the initial conditions used in the LVC/SH dynamics, based on a Wigner distribution around the Franck-Condon (FC) geometry and the LVC model potentials. Diabatic state character calculated from a transition-density matrix analysis.

An interesting question is if it is possible to find simple descriptors of the system that can predict (parts of) its photodynamics mechanism. To do this, we analyze the density of states (DOS) around the Franck-Condon geometry in the diabatic basis based on the transition-density matrix analysis. In Figure 5 in the main paper we have already analyzed the diabatic character of the electronic states directly at the Franck-Condon geometry. In Figure S11, this analysis is expanded to geometries around the Franck-Condon geometry by considering the ensemble of 10000 structures sampled from the Wigner distribution that was used to initialize the nonadiabatic dynamics. This Wigner ensemble includes the nuclear motion of the molecule in its ground state and the large number of samples allows to obtain a smooth distribution of the state characters.

As can be seen in Figure S11(a) for range-separation parameters of set A, the singlet

DOS (positive axis) below 2.5 eV is dominated by $^1$MLCT character (orange area), while $^1$MC states (red area) are found above 2.5 eV. Since we start our dynamics by excitation between 1.0-2.5 eV, mostly $^1$MLCT states were initially populated, recall Figure 7(e) in the main paper. Among the triplet states (negative axis), most DOS below 2.0 eV is given by $^3$MLCT states (dark blue area). $^3$MC DOS (violet curve) is found between energies of 1.5 and 2.5 eV, and above 2.5 eV, the largest triplet DOS contributions are given $^3$LC (turquois area). While $^3$MC DOS is also found within the excitation energy window of 1.0-2.5 eV, it is less than the $^3$MLCT DOS and, more importantly, it does not reach as far down in energy as that of the $^3$MLCT state. This distribution is mirrored by the dynamics, that mainly populate $^3$MLCT states [Figure 7(e)].

In Figure S11(b), the diabatic DOS is shown for the range-separation parameters of set B. While the comparison to the TAS results indicates that the (0.2; 0.08) set does not yield the potential energy surfaces of all states correctly, we can still test if analyzing its DOS can predict the corresponding mechanism. In the singlet domain, DOS from both the $^1$MLCT and $^1$MC states is found between energies of 1.5-3.0 eV with a rather constant ration of 2:1. This ratio is also found in the initial singlet populations [Figure 7(f)], and was maintained throughout the dynamics. Among the triplet states, the largest DOS below energies of 2.5 eV is still given by the $^3$MLCT –as was for the (0.0; 0.14) range-separation parameters. However, the amount of $^3$MC DOS at these energies is now comparable, and especially at energies below 1.75 eV, the $^3$MC DOS is even larger than that of the $^3$MLCT states. Similarly, the diabatic triplet populations during the dynamics showed almost equal contributions of $^3$MC and $^3$MLCT states.

Analyzing the density of states also seems to predict the course of the set B dynamics well. However, this applies only to the initial processes occuring close to the Franck-Condon geometry. For example, there is no $^3$MC DOS reaching further down to lower energies that could explain the intersystem crossing back to the ground state $S_0$. As discussed in Section 4.3 in the main paper, population of MC states leads to displacements in the metal-ligand bond lengths. Processes involving MC states occur in regions, for which the DOS sampled around the Franck-Condon geometry is not an adequate representation anymore. Thus, predicting the outcome of excited-state dynamics based on analyzing the DOS around the Franck-Condon geometry is not straightforward without the knowledge already established from the dynamics simulations.

# S5 Testing the Accuracy of the LVC Potentials

## S5.1 Normal-Mode Scans

The LVC/SH simulations using the Set B parameters resulted in trajectories undergoing differences in Fe−N bond lengths of up to 0.10-0.15 Å. As the LVC potentials are expressed in the basis of the harmonic normal modes of the electronic ground state, these large displacements could possibly lead to regions of the potential energy surface with anharmonicity. In this case, the LVC potentials may not be a good approximation of the underlying TDDFT reference potentials anymore.

In order to test this scenario, we have computed potential energy scans along a number of normal modes using both the Set B TDDFT level of theory as well as the thereof derived LVC model. In particular, scans were performed along the normal modes 19 (135.21 $\mathrm{cm}^{-1}$), 23 (169.96 $\mathrm{cm}^{-1}$), 25 (194.95 $\mathrm{cm}^{-1}$), 26 (203.06 $\mathrm{cm}^{-1}$), 27 (207.96 $\mathrm{cm}^{-1}$), and 28 (230.91 $\mathrm{cm}^{-1}$), which corresponded to the six modes with the largest change in Fe−N bond lengths. The resulting curves for the lowest 9 singlet states (including the ground state) as well as the 14 lowest triplet states are shown in Figure S12, where TDDFT and LVC curves are drawn as solid lines and dashed lines respectively. In addition, we show the time evolution of the average displacement of all trajectories during the 2 ps surface hopping simulation for each normal mode as a black line and its standard deviation as a gray area.

As can be seen in Figure S12, the ground-state LVC curve coincides with the TDDFT reference for displacements of ±2 a.u. For more pronounced displacements, the LVC curves underestimate the TDDFT energies due a smaller curvature. However, geometries with larger displacements are rarely reached by the trajectories in the surface hopping simulations as both the average plus standard deviation of the displacements are typically restricted to the range of ±2. The only exception for this behavior among the selected modes is given by mode 23, where the average oscillates between −2 and 0 a.u., while the average plus standard deviation increases this range to ca. −4 and 0 a.u. Thus, we can conclude, that

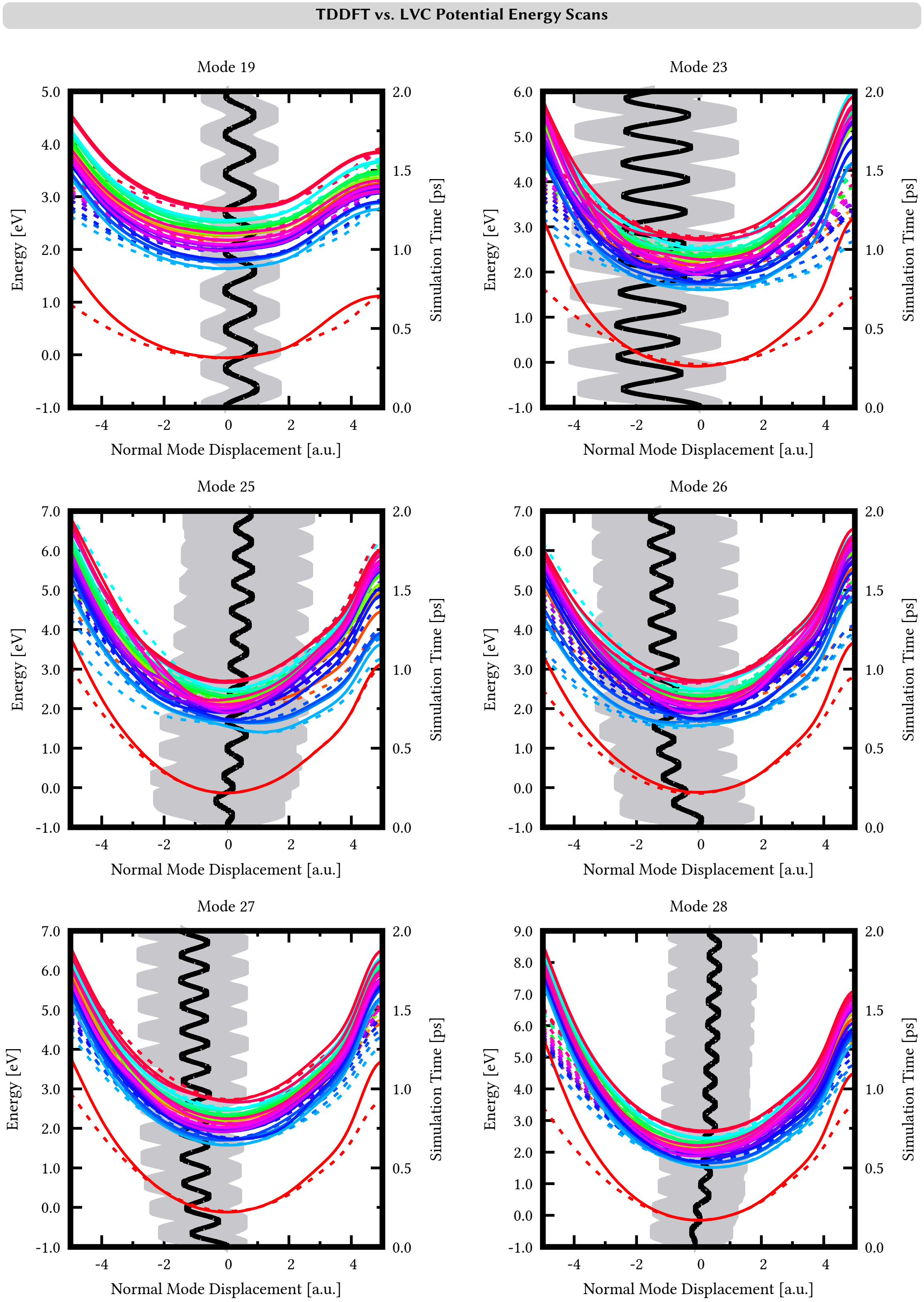

Figure S12: Overlay of TDDFT (solid line) vs. LVC (dashed lines) potential energy curves (colorful lines) and time evolution of average (black line) as well standard deviation (grey areas) of the normal-mode displacement of the trajectories from the Set B simulations for six normal describing Fe-N bond elongation. Ground-state and excited-state curves.

the ground-state potential is in general well described by the LVC model for the geometries that are traversed in the dynamics. For the large displacements of $-4$ a.u. of mode 23, the difference between LVC and DFT potentials is ca. 0.6 eV; it is there, however, also of similar size for the excited states, thus, leaving only a small error in relative energies.

At energies of 2 eV above the electronic ground state lies a dense region of singlet and triplet excited states. In order to better see the differences between LVC and TDDFT potentials for these states, we show selected parts of the curves in Figure S13. As can be seen, for modes 19, 27, and 28 –which appear harmonic in the selected displacement range –LVC and TDDFT curves agree well. The energetic differences reach 0.1 eV for some states at the edges of the shown displacement range, however, they are typically much smaller at all other displacements shown. For mode 23, which also shows harmonic potentials (see full range in Figure S12), there is expectantly close agreement between LVC and TDDFT curves around the equilibrium geometry. However, larger energetic differences of up to 0.2 eV are reached at larger negative displacements ($< -2$ a.u.) for some of the excited states.

For modes 25 and 26, Figure S13 shows a combination of harmonic and anharmonic TDDFT potentials. While the harmonic potentials are again well reproduced in the LVC model, the situation is more nuanced for the anharmonic potentials, where the LVC model is able to capture some of features but misses others. For example, for the lowest excited states (blue-violet lines) of the mode 25 scan, the potentials are well reproduced at positive displacements. In contrast, at negative displacements, the energy difference between the two lowest excited TDDFT potential curves decreases, while this difference increases in the LVC model. However, the average displacement of the trajectories tends towards positive values where also the minimum of the lowest excited stays lies, and in this displacement range, the LVC potentials agree well with the TDDFT ones.

Concluding, this analysis suggests that the LVC potentials can in general describe the reference TDDFT potentials of the complex $[\mathrm{Fe(cpmp)_2}]^{2+}$well, at least, for geometries that are actually reached in the surface hopping dynamics simulations. At certain, very displaced

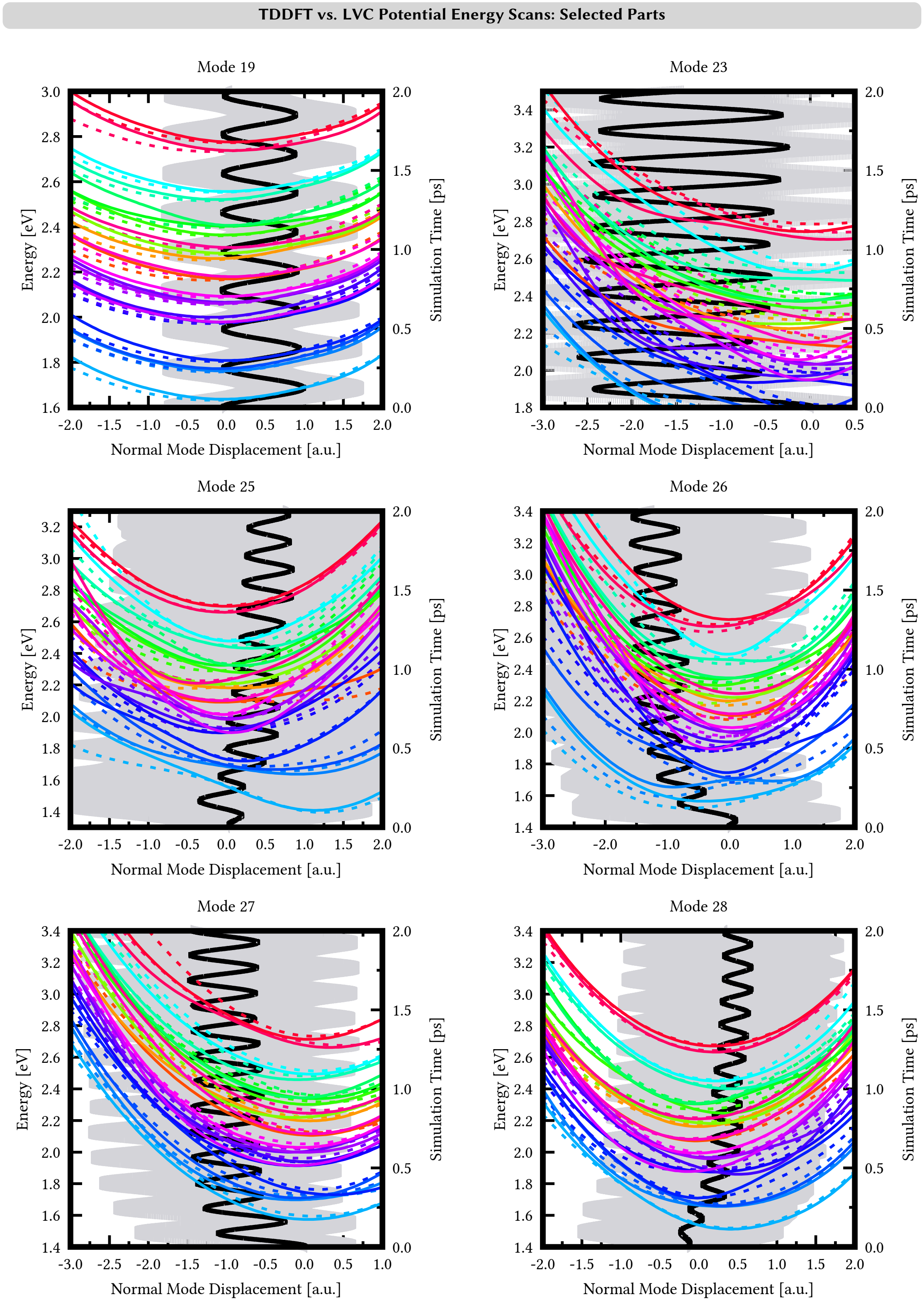

Figure S13: Overlay of TDDFT (solid line) vs. LVC (dashed lines) potential energy curves (colorful lines) and time evolution of average (black line) as well standard deviation (grey areas) of the normal-mode displacement of the trajectories from the Set B simulations for six normal describing Fe-N bond elongation. Focus on excited-state curves.

geometries, energetic differences between LVC and TDDFT potentials can become ca. 0.2 eV, however, the differences are typically much smaller and of the order of $< 0.1$ eV. Finally, the analysis further shows, that while the LVC potentials are formulated in the basis of the harmonic normal modes of the electronic ground states, LVC potentials can display certain anharmonic features due to the inclusion of state-state coupling elements.

## S5.2 Internal Conversion from $S_1$ to Hot Ground-State $S_0^*$

The TSH/LVC dynamics of the Set B simulations showed internal conversion from the $S_1$ state to a hot ground state $S_0^*$. Such a process is possible due to non-adiabatic couplings between the two states. These couplings are largest in the vicinity of a conical intersection, where state transfer is consequently most efficient. In surface hopping dynamics, the exact geometries of conical intersections are rarely hit when simulating polyatomic molecules. However, molecules still come to points with small energy differences between the coupled states, thus, coming close to a conical intersection. In a simplified picture, the $S_1 \rightarrow S_0$ internal conversion is thus mediated by a $S_{1/}S_0$ conical intersection. In principle, LVC models can describe the correct shape of conical intersections.[72] However, the reference method used in the current study, TDDFT, is not capable of describing $S_{1/}S_0$ conical intersections correctly.[73] It is, thus, interesting to investigate the $S_1 \rightarrow S_0$ internal conversion in the TSH/LVC simulations in more detail. For this, we have re-calculated the potential energies of an example trajectory using the set B LC-BLYSP functional and compare them with the LVC potential energy curves in Figure S14.

As can be seen, while some the general trends of the LVC trajectory (Figure S14(a)) such as the simultaneous rise and fall of the states due to the nuclear motion are also found when re-computing the potential energies with TDDFT (Figure S14(b)), there are some differences in the relative energies between the states. Most notable, TDDFT excitation energies are larger than LVC excitation energies, which appears to be most prominent for the $S_1$ state (red curve). The LVC trajectory hops from the $S_1$ state to the $S_0$ state at $t = 623$ fs, see Figure S14(a). At this time step, the energy difference between the $S_1$ and $S_0$ states in the

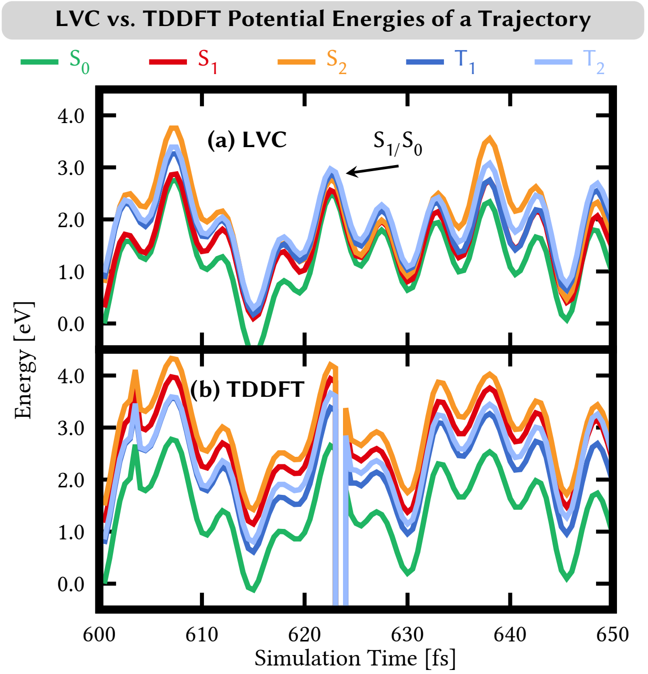

Figure S14: Comparison of lowest-excited states computed with (a) LVC and (b) TDDFT (set B) along an example trajectory. The relative energies were set to zero for the ground-state energy in the first time step ($t = 0$ fs).

LVC model is 0.08 eV. Using TDDFT, the energy gap is much larger, amounting to 1.29 eV. This large discrepancy, however, is due to the inability to describe this region of the potential energy surface correctly. Already at the next time step, $t = 623.5$ fs, the (TD)DFT calculations –at the geometry taken from the LVC trajectory –converges to a very different result, where the ground-state DFT energy drops from a value of $-3176.232585$ a.u. to a value of $-4785.064624$ a.u., clearly indicating a serious problem of the DFT calculation. At the following time step ($t = 624.0$ fs), the DFT energies reaches again a reasonable value of $-3176.260653$ a.u. At $t = 623.5$ fs, the $S_1/S_0$ TDDFT energy difference dropped to 0.51 eV, while it returns to 1.28 eV at $t = 624.0$ fs. In contrast to the extreme changes in the (TD)DFT energies, the LVC potentials follow an orderly progression with the $S_1/S_0$ LVC energy gap changing only slightly to 0.10 and 0.12 eV at the time steps following the hop. This example thus shows the peculiar case where the LVC potentials might compensate for errors in the TDDFT potentials near the $S_{1/}S_0$ conical intersection. This assumption is difficult to test without further reference calculations using multi-reference methods such as CASPT2, which come for [Fe(cpmp)$_2$]$^{2+}$unfortunately with prohibitively large computational costs.

Concluding this analysis, thus, suggests, that in the case where a $S_{1/}S_0$ conical intersection could be reached by LVC extrapolation from the TDDFT reference potentials from the Franck-Condon reference geometry, the LVC methods actually provides a way to bypass the deficiencies of (TD)DFT at this point. The effect of using LVC model potentials on the observed reaction mechanism in set B simulations appears to cancel out the error introduced by TDDFT near the $S_{1/}S_0$ degeneracies for [Fe(cpmp)$_2$]$^{2+}$.

## S6 Transient Absorption Spectroscopy of [Fe(cpmp)$_2$]$^{2+}$

Transient absorption spectra of [Fe(cpmp)$_2$]$^{2+}$were recorded with a time resolution of about 100 fs by a pump-probe setup in which tunable ultrashort laser pulses generated by a non-collinear optical parametric amplifier (NOPA) are used for excitation and a white light continuum for probing.[74] The NOPA and the white light stage featuring a CaF2 crystal are pumped by a regenerative Ti:sapphire amplifier system (CPA 2001, Clark MXR, Inc.) operating at a center wavelength of 775 nm and a repetition rate of 1 kHz. The excitation pulses had a center wavelength of 620 nm and their dispersion was controlled by a prism compressor. The polarizations of pump and probe were set to magic angle to avoid signal contributions due to orientational relaxation. The beams were focused onto the sample to overlapping spots with diameters of 345 µm for the pump and 150 µm for the probe. After the sample, the probe was dispersed by a prism and the transmission changes were spectrally resolved recorded by a CCD array detector. As sample served an acetonitrile solution of [Fe(cpmp)$_2$]$^{2+}$(PF$_6$)$_2$ which was filled into a 1 mm thick fused silica cuvette. The compound was generously provided by Prof. Katja Heinze and coworkers from the Johannes Gutenberg University Mainz.

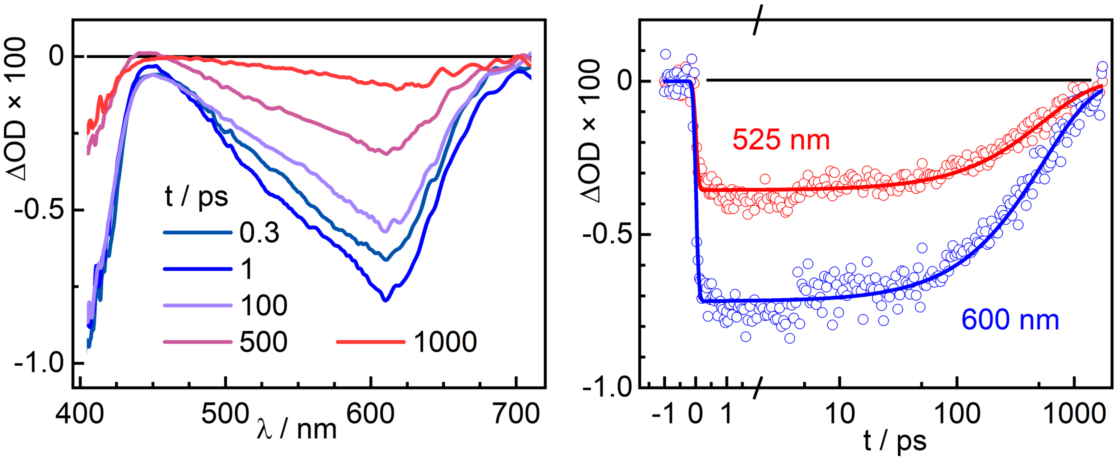

Figure S15: Left panel: Selected transient absorption spectra of [Fe(cpmp)$_2$]$^{2+}$in acetonitrile after optical excitation at 620 nm. The delay times of the spectra are given in the legend. Right panel: Time traces of the transient absorption probed at 525 nm (red circles) and at 600 nm (blue circles). The solid lines represent kinetic traces of an exponential global fit which reveals a decay time of 550 ps.

Transient absorption spectra after optical excitation of [Fe(cpmp)$_2$]$^{2+}$dissolved in acetonitrile are shown for selected delay times in Figure S15. They are completely dominated by the ground state bleach (GSB) which reflects the missing ground state absorption of molecules in excited states. Accordingly its shape resembles the inverse of the steady state absorption spectrum. The GSB appears with the time resolution of the experiment and decays then on the sub-nanosecond scale. A global monoexponential signal decay was fitted to the transient absorption data and revealed a decay time of 550 ps. In Figure S15 time traces of the transient absorption at 525 nm and 600 nm are compared to the corresponding fit traces showing that the monoexponential decay reproduces the data within the experimental accuracy. The results indicate that after optical excitation of the low lying singlet MLCT states intersystem crossing and relaxation to the lowest electronically excited triplet states occurs very quickly and is not resolved in our measurements. In these states the molecules stay for 550 ps until they return to the ground state.

# References

(1) Becke, A. D. Density-functional thermochemistry. III. The role of exact exchange. *J. Chem. Phys.* **1993**, *98*, 5648–5652.

(2) Weigend, F.; Ahlrichs, R. Balanced basis sets of split valence, triple zeta valence and quadruple zeta valence quality for H to Rn: Design and assessment of accuracy. *Phys. Chem. Chem. Phys.* **2005**, *7*, 3297.

(3) Weigend, F. Accurate Coulomb-fitting basis sets for H to Rn. *Phys. Chem. Chem. Phys.* **2006**, *8*, 1057.

(4) Petersson, G. A.; Bennett, A.; Tensfeldt, T. G.; Al-Laham, M. A.; Shirley, W. A.; Mantzaris, J. A complete basis set model chemistry. I. The total energies of closed-shell atoms and hydrides of the first-row elements. *J. Chem. Phys.* **1988**, *89*, 2193–2218.

(5) Petersson, G. A.; Al-Laham, M. A. A complete basis set model chemistry. II. Open-shell systems and the total energies of the first-row atoms. *J. Chem. Phys.* **1991**, *94*, 6081–6090.

(6) Frisch, M. J.; Trucks, G. W.; Schlegel, H. B.; Scuseria, G. E.; Robb, M. A.; Cheeseman, J. R.; Scalmani, G.; Barone, V.; Petersson, G. A.; Nakatsuji, H.; Li, X.; Caricato, M.; Marenich, A. V.; Bloino, J.; Janesko, B. G.; Gomperts, R.; Mennucci, B.; Hratchian, H. P.; Ortiz, J. V.; Izmaylov, A. F.; Sonnenberg, J. L.; Williams-Young, D.; Ding, F.; Lipparini, F.; Egidi, F.; Goings, J.; Peng, B.; Petrone, A.; Henderson, T.; Ranasinghe, D.; Zakrzewski, V. G.; Gao, J.; Rega, N.; Zheng, G.; Liang, W.; Hada, M.; Ehara, M.; Toyota, K.; Fukuda, R.; Hasegawa, J.; Ishida, M.; Nakajima, T.; Honda, Y.; Kitao, O.; Nakai, H.; Vreven, T.; Throssell, K.; Montgomery, J. A., Jr.; Peralta, J. E.; Ogliaro, F.; Bearpark, M. J.; Heyd, J. J.; Brothers, E. N.; Kudin, K. N.; Staroverov, V. N.; Keith, T. A.; Kobayashi, R.; Normand, J.; Raghavachari, K.; Rendell, A. P.; Burant, J. C.; Iyengar, S. S.; Tomasi, J.; Cossi, M.; Millam, J. M.; Klene, M.;

Adamo, C.; Cammi, R.; Ochterski, J. W.; Martin, R. L.; Morokuma, K.; Farkas, O.; Foresman, J. B.; Fox, D. J. Gaussian 16 Revision C.01. **2016**,

(7) Shao, Y.; Gan, Z.; Epifanovsky, E.; Gilbert, A. T.; Wormit, M.; Kussmann, J.; Lange, A. W.; Behn, A.; Deng, J.; Feng, X.; Ghosh, D.; Goldey, M.; Horn, P. R.; Jacobson, L. D.; Kaliman, I.; Khaliullin, R. Z.; Kuś, T.; Landau, A.; Liu, J.; Proynov, E. I.; Rhee, Y. M.; Richard, R. M.; Rohrdanz, M. A.; Steele, R. P.; Sundstrom, E. J.; Woodcock, H. L.; Zimmerman, P. M.; Zuev, D.; Albrecht, B.; Alguire, E.; Austin, B.; Beran, G. J. O.; Bernard, Y. A.; Berquist, E.; Brandhorst, K.; Bravaya, K. B.; Brown, S. T.; Casanova, D.; Chang, C.-M.; Chen, Y.; Chien, S. H.; Closser, K. D.; Crittenden, D. L.; Diedenhofen, M.; DiStasio, R. A.; Do, H.; Dutoi, A. D.; Edgar, R. G.; Fatehi, S.; Fusti-Molnar, L.; Ghysels, A.; Golubeva-Zadorozhnaya, A.; Gomes, J.; Hanson-Heine, M. W.; Harbach, P. H.; Hauser, A. W.; Hohenstein, E. G.; Holden, Z. C.; Jagau, T.-C.; Ji, H.; Kaduk, B.; Khistyaev, K.; Kim, J.; Kim, J.; King, R. A.; Klunzinger, P.; Kosenkov, D.; Kowalczyk, T.; Krauter, C. M.; Lao, K. U.; Laurent, A. D.; Lawler, K. V.; Levchenko, S. V.; Lin, C. Y.; Liu, F.; Livshits, E.; Lochan, R. C.; Luenser, A.; Manohar, P.; Manzer, S. F.; Mao, S.-P.; Mardirossian, N.; Marenich, A. V.; Maurer, S. A.; Mayhall, N. J.; Neuscamman, E.; Oana, C. M.; Olivares-Amaya, R.; O'Neill, D. P.; Parkhill, J. A.; Perrine, T. M.; Peverati, R.; Prociuk, A.; Rehn, D. R.; Rosta, E.; Russ, N. J.; Sharada, S. M.; Sharma, S.; Small, D. W.; Sodt, A.; Stein, T.; Stück, D.; Su, Y.-C.; Thom, A. J.; Tsuchimochi, T.; Vanovschi, V.; Vogt, L.; Vydrov, O.; Wang, T.; Watson, M. A.; Wenzel, J.; White, A.; Williams, C. F.; Yang, J.; Yeganeh, S.; Yost, S. R.; You, Z.-Q.; Zhang, I. Y.; Zhang, X.; Zhao, Y.; Brooks, B. R.; Chan, G. K.; Chipman, D. M.; Cramer, C. J.; Goddard, W. A.; Gordon, M. S.; Hehre, W. J.; Klamt, A.; Schaefer, H. F.; Schmidt, M. W.; Sherrill, C. D.; Truhlar, D. G.; Warshel, A.; Xu, X.; Aspuru-Guzik, A.; Baer, R.; Bell, A. T.; Besley, N. A.; Chai, J.-D.; Dreuw, A.; Dunietz, B. D.; Furlani, T. R.; Gwaltney, S. R.; Hsu, C.-P.; Jung, Y.; Kong, J.; Lambrecht, D. S.; Liang, W.; Ochsenfeld, C.; Rassolov, V. A.;

Slipchenko, L. V.; Subotnik, J. E.; Van Voorhis, T.; Herbert, J. M.; Krylov, A. I.; Gill, P. M.; Head-Gordon, M. Advances in Molecular Quantum Chemistry Contained in the Q-Chem 4 Program Package. *Mol. Phys.* **2015**, *113*, 184–215.

(8) Gilbert, A. T. B.; Besley, N. A.; Gill, P. M. W. Self-Consistent Field Calculations of Excited States Using the Maximum Overlap Method (MOM). *J. Phys. Chem. A* **2008**, *112*, 13164–13171.

(9) Plasser, F. TheoDORE: A toolbox for a detailed and automated analysis of electronic excited state computations. *J. Chem. Phys.* **2020**, *152*, 084108.

(10) Tomasi, J.; Mennucci, B.; Cammi, R. Quantum Mechanical Continuum Solvation Models. *Chem. Rev.* **2005**, *105*, 2999–3093.

(11) Bokareva, O. S.; Grell, G.; Bokarev, S. I.; Kühn, O. Tuning Range-Separated Density Functional Theory for Photocatalytic Water Splitting Systems. *J. Chem. Theor. Comp.* **2015**, *11*, 1700–1709.

(12) de Queiroz, T. B.; Kümmel, S. Tuned Range Separated Hybrid Functionals for Solvated Low Bandgap Oligomers. *J. Chem. Phys.* **2015**, *143*, 034101.

(13) Livshits, E.; Baer, R. A Density Functional Theory for Symmetric Radical Cations from Bonding to Dissociation. *Phys. Chem. Chem. Phys.* **2007**, *9*, 2932–41.

(14) Karolewski, A.; Kronik, L.; Kümmel, S. Using Optimally Tuned Range Separated Hybrid Functionals in Ground-State Calculations: Consequences and Caveats. *J. Chem. Phys.* **2013**, *138*, 204115.

(15) Fdez. Galván, I.; Vacher, M.; Alavi, A.; Angeli, C.; Aquilante, F.; Autschbach, J.; Bao, J. J.; Bokarev, S. I.; Bogdanov, N. A.; Carlson, R. K.; Chibotaru, L. F.; Creutzberg, J.; Dattani, N.; Delcey, M. G.; Dong, S. S.; Dreuw, A.; Freitag, L.; Frutos, L. M.; Gagliardi, L.; Gendron, F.; Giussani, A.; González, L.; Grell, G.; Guo, M.;

Hoyer, C. E.; Johansson, M.; Keller, S.; Knecht, S.; Kovačević, G.; Källman, E.; Li Manni, G.; Lundberg, M.; Ma, Y.; Mai, S.; Malhado, J. P.; Malmqvist, P. Å.; Marquetand, P.; Mewes, S. A.; Norell, J.; Olivucci, M.; Oppel, M.; Phung, Q. M.; Pierloot, K.; Plasser, F.; Reiher, M.; Sand, A. M.; Schapiro, I.; Sharma, P.; Stein, C. J.; Sørensen, L. K.; Truhlar, D. G.; Ugandi, M.; Ungur, L.; Valentini, A.; Vancoillie, S.; Veryazov, V.; Weser, O.; Wesołowski, T. A.; Widmark, P.-O.; Wouters, S.; Zech, A.; Zobel, J. P.; Lindh, R. OpenMolcas: From Source Code to Insight. *J. Chem. Theor. Comp.* **2019**, *15*, 5925–5964.

(16) Aquilante, F.; Boman, L.; Boström, J.; Koch, H.; Lindh, R.; de Merás, A. S.; Pedersen, T. B. In *Linear-Scaling Techniques in Computational Chemistry and Physics: Methods and Applications*; Zalesny, R., Papadopoulos, M. G., Mezey, P. G., Leszczynski, J., Eds.; Springer Netherlands: Dordrecht, 2011; pp 301–343.

(17) Roos, B. O.; Lindh, R.; Malmqvist, P.-Å.; Veryazov, V.; Widmark, P.-O. Main group atoms and dimers studied with a new relativistic ANO basis set. *J. Phys. Chem. A* **2004**, *108*, 2851–2858.

(18) Roos, B. O.; Lindh, R.; Malmqvist, P.-Å.; Veryazov, V.; Widmark, P.-O. New Relativistic ANO Basis Sets for Transition Metal Atoms. *J. Phys. Chem. A* **2005**, *109*, 6575–6579.

(19) Douglas, M.; Kroll, N. M. Quantum electrodynamical corrections to the fine structure of helium. *Ann. Phys.* **1974**, *82*, 89–155.

(20) Ghigo, G.; Roos, B. O.; Malmqvist, P.-Å. A modified definition of the zeroth-order Hamiltonian in multiconfigurational perturbation theory CASPT2. *Chem. Phys. Lett.* **2004**, *396*, 142–149.

(21) Forsberg, N.; Malmqvist, P.-Å. Multiconfiguration perturbation theory with imaginary level shift. *Chem. Phys. Lett.* **1997**, *274*, 196–204.

(22) Köppel, H.; Domcke, W.; Cederbaum, L. S. In *Advances in Chemical Physics Vol. 57*; Prigogine, I., Rice, S. A., Eds.; John Wiley & Sons, 1984; pp 59–246.

(23) Plasser, F.; Gómez, S.; Menger, M. F. S. J.; Mai, S.; González, L. Highly efficient surface hopping dynamics using a linear vibronic coupling model. *Phys. Chem. Chem. Phys.* **2019**, *21*, 57–69.

(24) Zobel, J. P.; Heindl, M.; Plasser, F.; Mai, S.; González, L. Surface Hopping Dynamics on Vibronic Coupling Models. *Acc. Chem. Res.* **2021**, *54*, 3760–3771.

(25) Zobel, J. P.; Bokareva, O. S.; Zimmer, P.; Wölper, C.; Bauer, M.; González, L. Intersystem Crossing and Triplet Dynamics in Iron(II) N-Heterocyclic Carbene Photosensitizer. *Inorg Chem.* **2020**, *59*, 14666–14678.

(26) Heindl, M.; Hongyan, J.; Hua, S.-A.; Oelschlegel, M.; Meyer, F.; Schwarzer, D.; González, L. Excited-State Dynamics of $[\mathrm{Ru}(^{S-S}\mathrm{bpy})(\mathrm{bpy})_2]^{2+}$ to Form Long-Lived Localized Triplet States. *Inorg. Chem.* **2021**, *60*, 1672–1682.

(27) Mai, S.; Menger, M. F. S. J.; Marazzi, M.; Stolba, D. L.; Monari, A.; González, L. Competing ultrafast photoinduced electron transfer and intersystem crossing of $[\mathrm{Re(CO)_3}$ $(\mathrm{Dmp})(\mathrm{His124})(\mathrm{Trp122})]^+$ in *Pseudomonas aeruginosa azurin*: a nonadiabatic dynamics study. *Theor. Chem. Acc.* **2020**, *139*, 65.

(28) Zobel, J. P.; Knoll, T.; González, L. Ultrafast and long-time excited state kinetics of an NIR-emissive vanadium(III) complex II. Elucidating Triplet-to-Singlet Excited-State Dynamics. *Chem. Sci.* **2021**, *12*, 10791–10801.

(29) Richter, M.; Marquetand, P.; González-Vázquez, J.; Sola, I.; González, L. SHARC: *ab initio* Molecular Dynamics with Surface Hopping in the Adiabatic Representation Including Arbitrary Couplings. *J. Chem. Theory Comput.* **2011**, *7*, 1253–1258.

(30) Mai, S.; Marquetand, P.; González, L. A General Method to Describe Intersystem Crossing in Trajectory Surface Hopping. *Int. J. Quant. Chem.* **2015**, *115*, 1215–1231.

(31) Mai, S.; Marquetand, P.; González, L. Nonadiabatic dynamics: the SHARC approach. *WIREs Comput. Mol. Sci.* **2018**, *8*, e1370.

(32) Mai, S.; Richter, M.; Heindl, M.; Menger, M. F. S. J.; Atkins, A.; Ruckenbauer, M.; Plasser, F.; Ibele, L. M.; Kropf, S.; Oppel, M.; Marquetand, P.; González, L. SHARC2.1: Surface Hopping Including Arbitrary Couplings –Program Package for Non-Adiabatic Dynamics. sharc-md.org, 2019.

(33) Iikura, H.; Tsuneda, T.; Yanai, T.; Hirao, K. A Long-Range Correction Scheme for Generalized-Gradient-Approximation Exchange Functionals. *J. Chem. Phys.* **2001**, *115*, 3540–3544.

(34) Hirata, S.; Head-Gordon, M. Time-dependent density functional theory within the Tamm-Dancoff approximation. *Chem. Phys. Lett.* **1999**, *314*, 291–299.

(35) Neese, F. Software update: the ORCA program system, version 4.0. *WIREs Comput. Mol. Sci.* **2018**, *8*, e1327.

(36) Ditchfield, R.; Hehre, W. J.; Pople, J. A. Self-Consistent Molecular-Orbital Methods. IX. An Extended Gaussian-Type Basis for Molecular-Orbital Studies of Organic Molecules. *J. Chem. Phys.* **1971**, *54*, 724–728.

(37) Hariharan, P. C.; Pople, J. A. The influence of polarization functions on molecular orbital hydrogenation energies. *Theor. Chim. Acta* **1973**, *28*, 213–222.

(38) Hehre, W. J.; Ditchfield, R.; Pople, J. A. Self-Consistend Molecular Orbital Methods. XII. Further Extensions of Gaussian-type Basis Sets for Use in Molecular Orbital Studies of Organic Molecules. *J. Chem. Phys.* **1972**, *56*, 2257–2261.

(39) Rassolov, V. A.; Pople, J. A.; Ratner, M. A.; Windus, T. L. 6-31G* basis set for atoms K through Zn. *J. Chem. Phys.* **1998**, *109*, 1223–1229.

(40) van Wüllen, C. Molecular density functional calculations in the regular relativistic approximation: Method, application to coinage metal diatomics, hydrides, fluorides and chlorides, and comparison with first-order relativistic calculations. *J. Chem. Phys.* **1998**, *109*, 392–399.

(41) Sun, L.; Hase, W. L. Comparison of classical and Wigner sampling of transition state energy level for quasiclassical trajectory chemical dynamics simulations. *J. Chem. Phys.* **2010**, *133*, 044313.

(42) Barbatti, M.; Grannuci, G.; Persico, M.; Ruckenbauer, M.; Vazdar, M.; Eckert-Maksić, M.; Lischka, H. The on-the-fly surface-hopping program system NEWTON-X: Application to ab initio simulation of the nonadiabatic photodynamics of benchmark systems. *J. Photochem. Photobiol. A* **2007**, *190*, 228–240.

(43) Granucci, G.; Persico, M.; Toniolo, A. Direct Semiclassical simulation of photochemical processes with semiempirical wave functions. *J. Chem. Phys.* **2001**, *114*, 10608–10615.

(44) Granucci, G.; Persico, M.; Zoccante, A. Including quantum decoherence in surface hopping. *J. Chem. Phys.* **2010**, *133*, 134111.

(45) Plasser, F.; Ruckenbauer, M.; Mai, S.; Oppel, M.; Marquetand, P.; González, L. Efficient and Flexible Computation of Many-Electron Wave-Function Overlaps. *J. Chem. Theory Comput.* **2016**, *12*, 1207–1219.

(46) Autschbach, J.; Srebro, M. Delocalization Error and "Functional Tuning" in Kohn–Sham Calculations of Molecular Properties. *Acc. Chem. Res.* **2014**, *47*, 2592–602.

(47) Egger, D. A.; Weissman, S.; Refaely-Abramson, S.; Sharifzadeh, S.; Dauth, M.; Baer, R.; Kümmel, S.; Neaton, J. B.; Zojer, E.; Kronik, L. Outer-Valence Electron Spectra of Prototypical Aromatic Heterocycles from an Optimally Tuned Range-Separated Hybrid Functional. *J. Chem. Theor. Comp.* **2014**, *10*, 1934–1952.

(48) Stein, T.; Kronik, L.; Baer, R. Reliable Prediction of Charge Transfer Excitations in Molecular Complexes Using Time-Dependent Density Functional Theory. *J. Amer. Chem. Soc.* **2009**, *131*, 2818–2820.

(49) Stein, T.; Kronik, L.; Baer, R. Prediction of Charge-Transfer Excitations in Coumarin-Based Dyes Using a Range-Separated Functional Tuned from First Principles. *J. Chem. Phys.* **2009**, *131*, 244119.

(50) Bokarev, S. I.; Bokareva, O. S.; Kühn, O. Electronic Excitation Spectrum of the Photosensitizer $[\mathrm{Ir(Ppy)_2(Bpy)}]^+$. *J. Chem. Phys.* **2012**, *136*, 214305.

(51) Bokarev, S. I.; Bokareva, O. S.; Kühn, O. A Theoretical Perspective on Charge Transfer in Photocatalysis. The Example of Ir-Based Systems. *Coord. Chem. Rev.* **2015**, *304-305*, 133–145.

(52) Fischer, S.; Bokareva, O. S.; Barsch, E.; Bokarev, S. I.; Kühn, O.; Ludwig, R. Mechanistic Study of Photocatalytic Hydrogen Generation with Simple Iron Carbonyls as Water Reduction Catalysts. *ChemCatChem* **2016**, *8*, 404–411.

(53) Bokareva, O.; Möhle, T.; Neubauer, A.; Bokarev, S.; Lochbrunner, S.; Kühn, O. Chemical Tuning and Absorption Properties of Iridium Photosensitizers for Photocatalytic Applications. *Inorganics* **2017**, *5*, 23.

(54) Friedrich, A.; Bokareva, O. S.; Luo, S.-P.; Junge, H.; Beller, M.; Kühn, O.; Lochbrunner, S. Effective Quenching and Excited-State Relaxation of a Cu(I) Photosensitizer Addressed by Time-Resolved Spectroscopy and TDDFT Calculations. *Chem. Phys.* **2018**, *515*, 557–563.

(55) Prokopiou, G.; Kronik, L. Spin-State Energetics of Fe Complexes from an Optimally Tuned Range-Separated Hybrid Functional. *Chem. Eur. J.* **2017**, 5173–5182.

(56) Lin, Z.; Van Voorhis, T. Triplet Tuning: A Novel Family of Non-Empirical Exchange–Correlation Functionals. *J. Chem. Theor. Comp.* **2019**, *15*, 1226–1241.

(57) Bokareva, O. S.; Baig, O.; Al-Marri, M. J.; Kühn, O.; González, L. The Effect of N-Heterocyclic Carbene Units on the Absorption Spectra of Fe(II) Complexes: A Challenge for Theory. *Phys. Chem. Chem. Phys.* **2020**, *22*, 27605–27616.

(58) Dierks, P.; Päpcke, A.; Bokareva, O. S.; Altenburger, B.; Reuter, T.; Heinze, K.; Kühn, O.; Lochbrunner, S.; Bauer, M. Ground- and Excited-State Properties of Iron(II) Complexes Linked to Organic Chromophores. *Inorg. Chem.* **2020**, *59*, 14746–14761.

(59) Zobel, J. P.; Bokareva, O. S.; Zimmer, P.; Wölper, C.; Bauer, M.; González, L. Intersystem Crossing and Triplet Dynamics in an Iron(II) N-Heterocyclic Carbene Photosensitizer. *Inorg. Chem.* **2020**, *59*, 14666–14678.

(60) Möhle, T.; Bokareva, O. S.; Grell, G.; Kühn, O.; Bokarev, S. I. Tuned Range-Separated Density Functional Theory and Dyson Orbital Formalism for Photoelectron Spectra. *J. Chem. Theor. Comp.* **2018**, *14*, 5870–5880.

(61) Perdew, J. P.; Parr, R. G.; Levy, M.; Balduz, J. L. Density-Functional Theory for Fractional Particle Number: Derivative Discontinuities of the Energy. *Phys. Rev. Lett.* **1982**, *49*, 1691–1694.

(62) Mori-Sánchez, P.; Cohen, A. J.; Yang, W. Localization and Delocalization Errors in Density Functional Theory and Implications for Band-Gap Prediction. *Phys. Rev. Lett.* **2008**, *100*, 146401.

(63) Dauth, M.; Caruso, F.; Kümmel, S.; Rinke, P. Piecewise Linearity in the GW Ap-

proximation for Accurate Quasiparticle Energy Predictions. *Phys. Rev. B* **2016**, *93*, 121115.

(64) Čížek, J. Stability Conditions for the Solutions of the Hartree?Fock Equations for Atomic and Molecular Systems. Application to the Pi-Electron Model of Cyclic Polyenes. *J. Chem. Phys.* **1967**, *47*, 3976.

(65) Bauernschmitt, R.; Ahlrichs, R. Treatment of electronic excitations within the adiabatic approximation of time dependent density functional theory. *Chem. Phys. Lett.* **1996**, *256*, 454–464.

(66) Casida, M. E.; Gutierrez, F.; Guan, J.; Gadea, F.-X.; Salahub, D. Charge-transfer correction for improved time-dependent local density approximation excited-state potential energy curves: Analysis within the two-level model with illustration for H2 and LiH . *J. Chem. Phys.* **2000**, *113*, 7062.

(67) Zobel, J. P.; Nogueira, J. J.; González, L. The IPEA Dilemma in CASPT2. *Chem. Sci.* **2017**, *8*, 1482–1499.

(68) Kepenekian, M.; Robert, V.; Le Guennic, B. What zeroth-order Hamlitonian for CASPT2 adiabatic energetics of Fe(II)$N_6$ architectures? *J. Chem. Phys.* **2009**, *131*, 114702.

(69) Rudavskyi, A.; Sousa, C.; de Graaf, C.; Havenith, R. W. A.; Broer, R. Computational approach to the study of thermal spin crossover phenomena. *J. Chem. Phys.* **2014**, *140*, 184318.

(70) Lawson Daku, L. M.; Aquilante, F.; Robinson, T. W.; Hauser, A. Accurate Spin-State Energetics of Transition Metal Complexes. 1. CCSD(T), CASPT2, and DFT Study of $[M(NCH)_6]^{2+}$ (M = Fe, Co). *J. Chem. Theory Comput.* **2012**, *8*, 4216–4231.

(71) Vela, S.; Fumanal, M.; Ribas-Ariño, J.; Robert, V. On the Zeroth-Order Hamiltonian for CASPT2 Calculations of Spin Crossover Compounds. *J. Comput. Chem.* **2016**, *37*, 947–953.

(72) Domcke, W., Yarkony, D. R., Köppel, H., Eds. *Conical Intersections*; World Scientific Publishing Co. Pte. Ltd., 2004.

(73) Tapavicza, E.; Tavernelli, I.; Rothlisberger, U.; Filippi, C.; Casida, M. E. Mixed time-dependent density-functional theory/classical trajectory surface hopping study of oxirane photochemistry. *J. Chem. Phys.* **2008**, *129*, 124108.

(74) Päpcke, A.; Friedrich, A.; Lochbrunner, S. Revealing the initial steps in homogeneous photocatalysis by time-resolved spectroscopy. *J. Phys. Condens. Matter* **2019**, *32*, 153001.